Astronomy & Astrophysics manuscript no. output
October 9, 2023

The SPHERE view of the Chamaeleon I star-forming region

The full census of planet-forming disks with GTO and DESTINYS programs

C. Ginski[1,2], R. Tazaki[2], M. Benisty[3], A. Garufi[4], C. Dominik[2], Á. Ribas[5], N. Engler[6], J. Hagelberg[7], R. G. van Holstein[5], T. Muto[8], P. Pinilla[9,10], K. Kanagawa[11], S. Kim[12], N. Kurtovic[9], M. Langlois[13], J. Milli[3], M. Momose[14], R. Orihara[14], N. Pawellek[15], T. O. B. Schmidt[16], F. Snik[1], and Z. Wahhaj[5]

[1] Leiden Observatory, Leiden University, P.O. Box 9513, 2300 RA Leiden, The Netherlands
e-mail: ginski@strw.leidenuniv.nl
[2] Anton Pannekoek Institute for Astronomy, University of Amsterdam, Science Park 904, 1098 XH Amsterdam, The Netherlands
[3] Univ. Grenoble Alpes, CNRS, IPAG, F-38000 Grenoble, France
[4] INAF, Osservatorio Astrofisico di Arcetri, Largo Enrico Fermi 5, I-50125, Firenze, Italy
[5] European Southern Observatory, Alonso de Córdova 3107, Vitacura, Casilla 19001, Santiago, Chile
[6] ETH Zurich, Institute for Particle Physics and Astrophysics, Wolfgang-Pauli-Strasse 27, 8093 Zurich, Switzerland
[7] Geneva Observatory, University of Geneva, 51 ch. Pegasi, 1290, Versoix, Switzerland
[8] Division of Liberal Arts, Kogakuin University, 1-24-2 Nishi-Shinjuku, Shinjuku-ku, Tokyo 163-8677, Japan
[9] Max-Planck-Institut für Astronomie, Königstuhl 17, 69117, Heidelberg, Germany.
[10] Mullard Space Science Laboratory, University College London, Holmbury St Mary, Dorking, Surrey RH5 6NT, UK.
[11] Department of Earth and Planetary Sciences, Tokyo Institute of Technology, 2-12-1 Ookayama, Meguro-ku, Tokyo 152-8551, Japan
[12] Department of Astronomy, Tsinghua University, Beijing 100084, China
[13] Centre de Recherche Astrophysique de Lyon, CNRS, UCBL, ENS Lyon, UMR 5574, F-69230, Saint-Genis-Laval, France
[14] College of Science, Ibaraki University, 2-1-1 Bunkyo, Mito, Ibaraki 310-8512, Japan
[15] Department of Astrophysics, University of Vienna, Türkenschanzstrasse 17, 1180 Vienna, Austria
[16] Hamburger Sternwarte, Gojenbergsweg 112, 21029, Hamburg, Germany

Received September 15, 1996; accepted March 16, 1997

ABSTRACT

Context. The past few years have seen a revolution in the study of circumstellar disks. New instrumentation in the near-infrared and (sub)-mm regime allowed us to routinely spatially resolve disk around stars in nearby star forming regions. As a result we found that sub-structures with scales of ∼10 au in disks are common. Yet we also revealed a zoo of different morphologies, sizes and luminosities, that is no less complex than the diversity of architectures found in evolved exoplanet systems.
Aims. We aim to study disk evolutionary trends as they appear in scattered light observations. Scattered light traces the small (micron-sized) particles at the disk surface that are well coupled to the gas. As such scattered light observations can be used to trace the distribution of the disk gas and its interaction with embedded perturbers.
Methods. We used VLT/SPHERE to observe 20 systems in the Cha I cloud in polarized scattered light in the near infrared. We combined the scattered light observations with existing literature data on stellar properties as well as with archival ALMA continuum data to study trends with system age and dust mass. We furthermore connect resolved near-infrared observations with the spectral energy distributions of the systems.
Results. In 13 of the 20 systems included in this study we detected resolved scattered light signals from circumstellar dust. For the CR Cha, CT Cha, CV Cha, SY Cha, SZ Cha and VZ Cha systems these are the first resolved observations of this kind. The observations found typically smooth and faint disks, with little sub-structure, with the notable exceptions of SZ Cha that shows an extended multiple ringed disk and WW Cha that shows interaction with the cloud environment. We resolve for the first time the stellar binary in the CS Cha system. Multiple wavelength observations of the disk around CS Cha revealed that the system contains small, compact dust grains which are strongly settled, consistent with numerical studies of circumbinary disks. We found that for our sample there exists a tentative correlation between relative disk-to-star brightness in scattered light and the presence of a dust cavity in the inner (unresolved) disk, as traced by the system SED. At the same time faint disks in our sample are generally younger than 2 Myr. We discuss an evolutionary pathway, traced by the scattered light observations, where young disks are self shadowed by their inner disks and faint, while older disks in the late stages of planet formation or around stellar binaries have opened a cavity and thus removed shadowing material close to the star.

Key words. Instrumentation: high angular resolution – Techniques: high angular resolution

1. Introduction

Circumstellar disks around young stars are the site of planet formation. The sizes, masses, and compositions of the planets as well as the architecture of the planetary systems being formed are a result of the properties of the planet-forming disks and the processes acting in these disks. It is however unclear yet how the statistics of planetary system architecture and planet popu-

lations relate to the observed properties of planet-forming disks. The past few years have seen a surge in spatially-resolved observations of such disks, using ALMA at sub-mm wavelengths and high-contrast imaging techniques at optical and near-IR wavelengths. Initially, these observations have focused on the largest and brightest disks, mostly around Herbig AeBe stars, for example the HD 135344 B system (Andrews et al. 2011; Muto et al. 2012; Garufi et al. 2014; van der Marel et al. 2016; Stolker et al. 2016), the HD 100546 system (Grady et al. 2001; Pineda et al. 2014; Walsh et al. 2014; Garufi et al. 2016) or the HD 97048 system (Walsh et al. 2016; Ginski et al. 2016; van der Plas et al. 2017a).

In the ALMA wavelength range a number of surveys of individual regions with limited spatial resolution and sensitivity have been carried out, for example Chameleon I (Pascucci et al. 2016), Lupus (Ansdell et al. 2016), σ Orionis (Ansdell et al. 2017), Taurus (Long et al. 2019) and Ophiuchus (Cieza et al. 2019). In near infrared scattered light such dedicated surveys of nearby star forming regions have so far been missing, with the majority of the field focusing on the study of individual objects. A first dedicated survey of T Tauri stars from multiple regions was carried out in the Disks around T Tauri Stars with SPHERE (DARTTS-S, Avenhaus et al. 2018; Garufi et al. 2020) program. Furtermore Garufi et al. (2018), conducted a large literature study, including 58 Herbig and T Tauri stars. However, all of these studies were inhomogeneous in the sense that they included systems from multiple star forming regions, which were biased toward bright and extended disks. Even so, their initial results suggest already some intriguing trends. Among other things they find an anti-correlation between the amount of near infrared excess and and the disk brightness in scattered light and the prevalence of spiral structures in older disks around more massive stars. However, to fully access the complementary information provided by scattered light and mm-wavelength observations we need now scattered light surveys of individual star forming regions.

In this study we present polarimetric scattered light observations of 10 members of the Chameleon I cloud (Cha I hereafter), conducted with VLT/SPHERE (Spectro-Polarimetric High-contrast Exoplanet REsearch, Beuzit et al. 2019). The Chameleon complex is one of only a few nearby star-forming regions that is ideally suited for the study of young stellar objects. Located at a distance of ~180±10 pc (Voirin et al. 2018), it is close enough that direct imaging observations are able to resolve circumstellar disks on spatial scales of a few au.

In the following section we describe the composition of the sample and put it in context of the young star population of Cha I. In section 3 we describe the observations and the data reduction. We then first discuss the polarization of the stellar light and its implications in section 4.1 and then describe the measurements taken in the polarimetric images, as well as global and individual disk properties in sections **??** and 5. We highlight the first resolved detection of the inner binary in the CS Cha system in section 5.2.2 and discuss our results in section 6.

2. Sample and stellar properties

Our sample consists of 20 members of Cha I, which we summarize in Table 1. The main selection criterion was the optical brightness of the targets (G < 13 mag), which allowed them to be used as natural guide stars for the SPHERE adaptive optics system. The sample contains 90% of the Cha I sources that can be observed by SPHERE. We are therefore nearly complete within the population of solar-like and intermediate-mass stars, with the aforementioned technical threshold translating into a stellar mass of approximately 0.5 $M_\odot$.

A large fraction of our targets (11 out of 20) is part of a stellar system. We illustrated the configuration of the systems in Table 1. The CS Cha and WW Cha systems feature a circumbinary disk. In both cases, the central stars are in tight orbits and the binary nature has been determined spectroscopically. The CT Cha, HP Cha, Sz41, and SZ Cha systems have a circumprimary disk configuration with wide, low-mass companions (which is itself a binary in HP Cha). DI Cha is a quadruple system with a close companion (named D) and a binary system (BC) at large separations. Finally, the CHX 22, WX Cha, and WY Cha systems are known close visual binaries with mass ratios closer to unity.

All stellar properties were computed based on the recent *Gaia* DR3 parallax (Gaia Collaboration et al. 2022). In four cases indicated in Table 1, the *Gaia* parallactic measurement is either uncertain or absent. Three of these cases are close binaries. The stellar masses and ages were computed through a set of PMS tracks (Siess et al. 2000; Bressan et al. 2012; Baraffe et al. 2015a; Choi et al. 2016) from the effective temperature and the stellar luminosity calculated from a Phoenix model of the stellar photosphere (Hauschildt et al. 1999) scaled to the de-reddened optical photometry from the literature. The mass accretion rates were calculated from the accretion luminosities updated to *Gaia* DR3 by Manara et al. (2016) using the usual relation of $\dot{M}_{acc} = 1.25\frac{L_{acc}R_*}{GM_*}$ (e.g. Hartmann et al. 1998). Finally, a crude estimate of the disk dust mass was derived from the ALMA fluxes at 887 μm by Pascucci et al. (2016) using the *Gaia* distance and the typical assumption (optically thin emission, dust temperature of 20 K, and dust opacity by Beckwith & Sargent 1991).

From Table 1, the bias in stellar mass due to the stellar optical brightness is clear, with 0.5 $M_\odot$ (for VZ Cha and WY Cha) being the lower end of the distribution and 2.4 $M_\odot$ (HD97048) the upper end. Conversely, the disk dust mass range is large as it spans from ~940 $M_\oplus$ (HD97048) to less than 1 $M_\oplus$ (CHX 22). In particular, our sample contains the four objects with the highest dust masses in Cha I (WW Cha, CR Cha, SZ Cha, CS Cha) based on Pascucci et al. (2016).

3. Observations and data reduction

Observations were carried out with the IRDIS (Infra-Red Dual-beam Imager and Spectrograph, Dohlen et al. 2008) and ZIMPOL (Zurich IMaging POLarimeter; Schmid et al. 2018) subsystems of VLT/SPHERE. IRDIS was operated in the dual-beam polarimetric imaging (DPI, Langlois et al. 2014) mode. This mode is used to detect linear polarization signals. For this purpose a half wave plate is used to rotate the astrophysical polarization signal in the frame of reference of two wire grid polarizers. The two perpendicular polarization directions are taken simultaneously, such that an ideal subtraction of the (unpolarized) stellar signal is possible. This observation mode is described in detail in de Boer et al. (2020) and van Holstein et al. (2020).

A detailed overview of the observation setup and atmospheric conditions is given in Appendix A. Single star targets, or systems with very low mass companions were generally observed with a coronagraph in place, obscuring the central star. In all but one case we used the N_ALC_YJH_S coronagraph for this purpose, which has a nominal inner working angle of 92.5 mas (Martinez et al. 2009; Carbillet et al. 2011). Since CV Cha was observed in J-band we used the N_ALC_YJ_S coronagraph (optimized for shorter wavelengths), which has a slightly smaller inner work-

Table 1: Properties of the sample. Columns are: target name, distance from *Gaia* DR3, stellar mass, crude estimate of the disk dust mass, mass accretion rate, age, and possible multiplicity of the target. The detailed derivation of these parameters is described in Sect. 2.

Target	d [pc]	M_* [$M_\odot$]	M_{dust} [$M_\oplus$]	log $\dot{M}_{acc}$ [$M_\odot$/yr]	age [Myr]	Binary
CHX 18 N	191.6 ± 0.03	0.9	13	−7.52	0.8–1.0	(*)
CHX 22	191.2 (1)	1.9±0.1 / 0.6±0.1	<1	< −4.8	2.8–3.3	(**)
CR Cha	185.2 ± 0.4	1.4±0.1	198	−8.41	0.8–1.0	(*)
CS Cha	190 (2)	1.3±0.1 / 0.6±0.1	84	−7.99	3.0–5.3	(**)*
CT Cha	190.0 ± 0.4	0.9±0.2	50	−6.53	1.2–1.9	(*)*
CV Cha	191.8 ± 0.5	2.1±0.2	29	−7.26	1.3–1.5	(*)
DI Cha	189.0 ± 0.6	2.3±0.2	9	−7.39	0.6–0.9	(*)* + **
HD97048	184.4 ± 0.7	2.4±0.2	940	< −7.72	3.6–4.4	(*)
HP Cha	187.3±1.3	1.7±0.1	80	< −5.63	5.2–5.7	(*)(**)
PDS 51	190 (2)	0.9±0.1 / 0.7±0.1	2	−7.80	2.5–3.9	(**)
RX J1106.3-7721	177.9 (1)	2.9±0.3	–	–	1.0–1.4	(*)
SY Cha	180.7 ± 0.4	0.7±0.1	50	< −4.66	1.5–2.0	(*)
Sz 41	191.8 ± 0.4	0.6±0.1 / 0.5±0.1	<1	−7.38	0.4–0.7	(*)*
Sz 45	188.9 ± 0.6	0.6±0.1	10	−8.02	1.6–2.2	(*)
SZ Cha	190.2 ± 0.9	1.5±0.1	150	−7.56	1.5–1.8	(*)*
TW Cha	183.1 ± 0.4	0.7±0.1	23	−8.56	1.5–2.2	(*)
VZ Cha	191.1 ± 0.6	0.5±0.1	60	−7.14	1.1–1.5	(*)
WW Cha	188.8 ± 1.0	1.9±0.1	630	−6.28	0.2–0.5	(**)
WX Cha	190.6 (1)	0.5±0.1	10	−6.69	0.9–1.2	(*)*
WY Cha	174.5 (1)	0.7±0.1	3	−8.36	1.5–2.1	(*)* + *

Notes. (1): the *Gaia* parallactic measurement has a large renormalized unit weighting error (RUWE ≫ 2) pointing to a very uncertain solution. (2): no *Gaia* parallax is calculated, and a value of 190 pc is adopted.

ing angle of 72.5 mas. For the known binary systems with bright secondary stars WX Cha and WY Cha we did not employ a coronagraph, but rather used short detector integration times (DIT) to avoid saturation.

All data was reduced using the IRDAP (IRDIS Data reduction for Accurate Polarimetry[1]) pipeline. The data reduction package is described in detail in van Holstein et al. (2020) and will thus only be briefly summarized here. After initial baseline data reduction (sky-subtraction, flat-fielding, bad pixel masking), the images were centered using either a center calibration frame with calibrated satellite spots (coronagraphic data), or a Gaussian fit (non-coronagraphic data). Each polarimetric cycle was then reduced by creating single and double difference images from the individual Q^+,Q^-,U^+ and U^- images (signifying different rotation positions of the internal half wave plate). Instrumental polarization was then removed using a full Mueller Matrix model of the instrument + telescope (see de Boer et al. 2020 for details). After this step residual (astrophysical) stellar polarization could be measured and removed, using the method described by Canovas et al. (2011). This was done in order to remove as much stellar signal as possible in order to get a clear view of the surrounding circumstellar material.

The so created final Stokes Q and U images were then used to generate radial Stokes images Q_ϕ and U_ϕ, following Schmid et al. (2006), but with a flipped sign convention more appropriate for disk scattered light observations as discussed in de Boer et al. (2020). Q_ϕ contains as positive values all azimuthally aligned polarized signal and as negative values all radially aligned polarization signal. U_ϕ contains all polarization signal 45° offset from radial or azimuthal direction. Since a circumstellar disk will pre-dominantly show single scattering (unless viewed under very high inclinations), the Q_ϕ image contains most of the actual signal, while the U_ϕ image can in principle be regarded as a convenient noise map.

In addition to the IRDIS near infrared observations CS Cha polarimetric observations with SPHERE/ZIMPOL in the optical were performed on 2018 December 23 in imaging mode P1 and on 2019 January 20 in field-stabilized mode P2. Images were taken in the slow-polarimetry mode using different filters in two arms of ZIMPOL: the I_PRIM filter in the arm 1 and R_PRIM filter in the arm 2. The star was placed behind a semi-transparent coronagraphic mask (V_CLC_MT_WF) with a radius of 77.5 mas. In total, 20 polarimetric QU cycles (120 exposures with DIT = 10 s) were recorded during the first night and 4 QU cycles (32 exposures with DIT = 58 s) during the second night. Each cycle consisted of four consecutive measurements with different HWP offset angles of 0°, 22.5°, 45°, and 67.5° switching the Stokes parameters $+Q$, $-Q$, $+U$, and $-U$, respectively. At the beginning and the end of science observations flux measurements were performed with the star offset from the coronagraphic mask using the neutral density filter ND_4.0 and DIT = 20 s (first night) and DIT = 80 s (second night).

The ZIMPOL data were reduced with the data reduction pipeline developed at ETH Zurich. The preprocessing and calibration of raw frames included subtraction of the bias and dark frames, flat-

[1] https://irdap.readthedocs.io

Table 2: Degree and angle of linear polarization of the stellar light measured from the SPHERE/IRDIS observations. The CS Cha and HD 97048 data points were obtained in the J-band. For HP Cha we only consider the primary star in the system.

System	DoLP [%]	AoLP [°]
CHX 18 N	0.37±0.04	132.4±4.7
CHX 22	1.33±0.17	133.2±4.4
CR Cha	1.84±0.02	124.8±0.6
CS Cha	0.34±0.02	141.1±5.4
CT Cha	0.99±0.10	124.6±3.8
CV Cha	0.94±0.39	109.0±9.1
DI Cha	1.42±0.05	143.7±1.1
HD97048	1.40±0.25	132.4±5.3
HP Cha	0.63±0.10	168.3±3.6
PDS 51	3.16±0.16	129.4±1.3
RX J1106.3-7721	1.44±0.06	146.1±1.2
SY Cha	0.91±0.08	83.8±2.4
Sz 41	1.00±0.72	107.6±18.7
Sz 45	0.90±0.14	130.3±2.9
SZ Cha	1.37±0.03	118.8±0.2
TW Cha	0.43± 0.12	148.3±9.8
VZ Cha	0.41±0.01	141.4±5.3
WW Cha	1.11±0.04	164.2±0.9
WX Cha	1.97±0.28	134.7±5.6
WY Cha	0.27±0.02	131.8±3.7

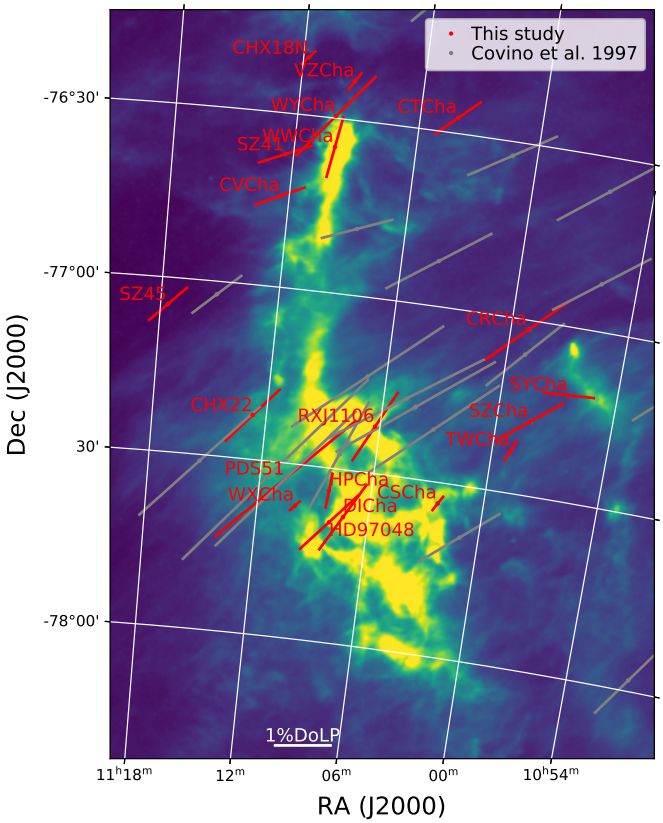

Fig. 1: Degree of linear polarization and angle of linear polarization of our target sources (red) and measurements by Covino et al. (1997) using background stars behind the Cha I cloud (grey). Optical measurements by Covino et al. (1997) where extrapolated to the near infrared regime by Serkowskis law. Polarization vectors are overlayed on a Herschel/SPIRE image at 160 μm showing the dust in the Cha I cloud.

fielding, and correction for the modulation and demodulation efficiency. The instrumental polarization was corrected through the forced normalization of the fluxes in the frames of two opposite polarization states measured in the annulus with inner radius of 100 pixels and outer radius of 200 pixels as described in (Engler et al. 2017). All frames were centered by fitting 2D Gaussian function to the intensity gradients of the stellar profile. The final format of the reduced Q and U images is 1024×1024 pixels with the pixel size approximately 3.6 × 3.6 mas on sky. The ZIMPOL data of CS Cha is discussed in section 5.2 and section 5.2.2.
In addition to the near-infrared and optical data we present complementary ALMA observations of the SY Cha systems. SY Cha was observed with ALMA in Band 6 during Cycle 6 as a part of project 2018.1.00689.S. The observations were done with the antenna configuration of C43-6 (15.25 min on source), C43-7 (15.25 min on source) and C43-9 (72.75 min on source) with the longest baseline of 16.2 km. The details of the observations and data reduction are presented in Orihara et al. (2022, submitted). In this paper, we present the continuum image at the central frequency of 225 GHz with the beam size of 0.″145×0.″109 and with the RMS noise level of 0.0175 mJy/beam.

4. Results on the global sample

In this section, we describe our sample as a whole. An analysis of the individual sources is given in Sect. 5. All the targets in our sample show some stellar (unresolved) polarization (see Sect. 4.1). However, resolved polarized light is detected in only 13 of the 20 targets. This signal is described in Sect. 4.2 and related to the disk and stellar properties in Sect. 4.3.

4.1. Stellar polarization

Following van Holstein et al. (2021), we used the IRDAP pipeline to measure the degree of linear polarization of the (unresolved) stellar light, which may also include a contribution from the inner disk regions (<8 au). We concentrated in all cases on the primary star in the system. The results are given in Table 2. In Figure 1, we overplotted the position of our target systems as well as the amount and angle of linear polarization on a Herschel/SPIRE map of the Cha I cloud complex (showing thermal dust emission at 160 μm). For comparison we plotted background stars (behind the Cha I cloud) with optical polarization measurements from Covino et al. (1997). Note that the angle of linear polarization is similar for all background stars. This is consistent with the stellar light being polarized interstellar dust grains, with the majority of the dust column density likely located in the Cha I cloud complex.

The majority (8 out of 10) of our target systems shows an angle of stellar polarization that is consistent with the background stars observed by Covino et al. (1997). This is an indication that in these systems the source of the polarized stellar light is likely dominated by the same mechanism, i.e. scattering of interstellar dust. The amount of stellar polarization is generally slightly lower than for the background stars observed by Covino et al. (1997). This can be due to the difference in wavelength, since linear polarization due to interstellar dust is typically lower in the near infrared (Serkowski et al. 1975) than in the optical. However, we also see a weak correlation with the distances of the individual systems listed in table 1. In particular the degree of linear polarization is the lowest for the CS Cha system and the WY Cha system, both of which have smaller distances than the

rest of the sample. This fits well with the picture that the majority of the interstellar polarization in the Covino et al. (1997) sample is induced as the light passes through the dense Cha I dust cloud. CS Cha and WY Cha, may the be located on the outer edges or slightly in front of the Cha I cloud complex given our line of sight.

Two systems, SY Cha and WW Cha, show significantly different angles of linear polarization than the remaining sample. This may indicate that the dominant source of linear polarization is not interstellar dust scattering, but rather is induced locally, i.e. at angular separations smaller than the resolution element of SPHERE in the H-band (~40 mas, i.e. inside of ~8 au). A possible explanation is an inner zone of the circumstellar disk. To cause a resulting polarization in the unresolved stellar light this inner part of the disk needs to be inclined, since otherwise (in a face-on oriented disk) different polarization directions would cancel each other out. This scenario is discussed in great detail in van Holstein et al. (2021). If the polarization signal is indeed caused by an unresolved inclined circumstellar disk, then the angle of polarization should be aligned with the minor axis of the disk, since the majority of the polarized light will be received from the disk ansae at scattering angles close to 90° (see van Holstein et al. (2021) for a radiative transfer model of such a configuration). We however need to caution that the degree of polarization that we measure for our target stars is likely a combination of local and interstellar effects. Thus detailed modelling of the local interstellar polarization would be necessary to derive constraints on the geometry of the inner disks in SY Cha and WW Cha. This is beyond the scope of this study. We also need to caution that for the other 8 systems we can in principle not rule out that there is additional local polarization of the stellar light, since the minor axis of an inner disk may by chance line up with the general direction of the local interstellar polarization.

!!DESTINYS sources to be added to this section!!

4.2. Disk geometry

As is clear from Fig. 2, some resolved polarized signal is detected in 13 of our 20 targets. In turn, 12 of these show a polarized light pattern consistent with a disk detection (with the only exception being CHX 22, see Zhang et al. 2023). The details of all individual systems are given in Sect. 5. Here, we extract the aspect ratio of the detected disk in order to define an overall trend for the sample.

The offset of ellipses, tracing iso-separation features on the disk, along the minor axis can be used to calculate the height of the $\tau = 1$ scattering surface of the disk as was shown in de Boer et al. (2016) and Ginski et al. (2016). While in the two aforementioned cases multiple rings were present, this is not typically the case for the disks in our sample (with the exception of HD 97048 and SZ Cha). However, we can still measure the offset of the ellipses that trace the outer edge of the disks as detected in scattered light, so determine the aspect ratio of the outermost region of the scattered light disk. We show in appendix C that this approach is valid, based on disk model images.

4.2.1. Fitting procedure

For the ellipse fit we follow two separate approaches for the ringed disks and those without such sub-structure. In both cases we use a sliding aperture, to extract radial profiles in azimuthal bins of 1°. The aperture size is chosen to reflect the resolution element in the images. for the ringed disks we fit 1d-Gaussian profiles to extract the ring locations from the radial profiles. For the disks without ringed sub-structure we trace the outer disk edge at which the disk signal drops below 3σ as determined from the image background. After the initial measurement we then bin the data in either case in azimuthal direction in increments of 10°. Note that in case of low signal-to-noise we excluded azimuthal disk regions for individual targets. For the uncertainties of the extracted data points we use the full-width-at-half-maximum (FWHM) of the Gaussian for the ring-like structures. For the data points that trace the disk edge we determine the slope of the radial profiles across the edge. The radial uncertainties Δr are then derived as:

$$\Delta r = \frac{3 * \delta F}{m_{\mathrm{profile}}} \quad (1)$$

With δF the standard deviation of the background flux in the image and m_{profile} the slope of the radial profile. A steep slope, i.e. a sharp disk edge leads to small uncertainties, while a small slope, i.e. a "fuzzy" disk edge leads to large uncertainties. For the azimuthal uncertainty we use a value of 0.1°, consistent with the calibration accuracy of our images. The extracted data points and associated uncertainties for both disk groups are shown in Figures C.3 and C.4.

We use the extracted data points for a two-step fitting process. Initially we use the least squares algorithm by Halíř & Flusser (1998) to find the best fitting ellipse, without any prior constraints to the disk parameters. These best fitting ellipses are overlayed in Figures C.3 and C.4. We determine the uncertainty of this fit with a least squares Monte Carlo (LSMC) approach. We repeat the fit 1e5 times. Each time we draw the location of each data point from a normal distribution with the width of the data points uncertainty. We then use the standard deviation of each ellipse parameter across all runs as the uncertainty for that parameter. The results of these initial fits are shown in Table 3. In appendix C we demonstrate that this approach reliably recovers the disk inclination and position angle if the disk inclination is larger than ~10°.

We then use a second step to refine the offset of the disk rings or outer disk edge from the stellar position. For this second step we constrain the disk inclination and position angle, either to literature measurements from ALMA mm observations (typically gas observations), or based on the prior fitting step when no ALMA data is available. We additionally constrain the ring or disk-edge semi-major axis to the value found in the previous step. We then only allow ellipse offsets from the stellar position along the minor axis, i.e. consistent with offsets introduced solely by the projected disk height and not by disk asymmetry. Based on these parameters we generate a grid of elliptical annuli (for the rings) or apertures (for disks without rings), with offsets along the minor axis increasing in steps of 0.1 pixel (1.25 mas). We then find the annulus or aperture for which the contained disk or ring flux is maximized. The uncertainties of the offset positions found in this way are found by finding the range of annulus or aperture positions within the flux uncertainty of the measurement. For the disk rings this is similar to the procedure employed to fit the ring locations for the HD 97048 system in Ginski et al. (2016). For the aspect ratio of the disk without rings we show the validity of this approach in appendix C. The offset and aspect ratio values found with this second fitting step are also given in Table 3. We note that for the faint disks around SZ 45, TW Cha and VZ Cha the uncertainty of the disk inclination or position angle was large and no complementary ALMA data was available, thus we omitted the second fitting step in these cases.

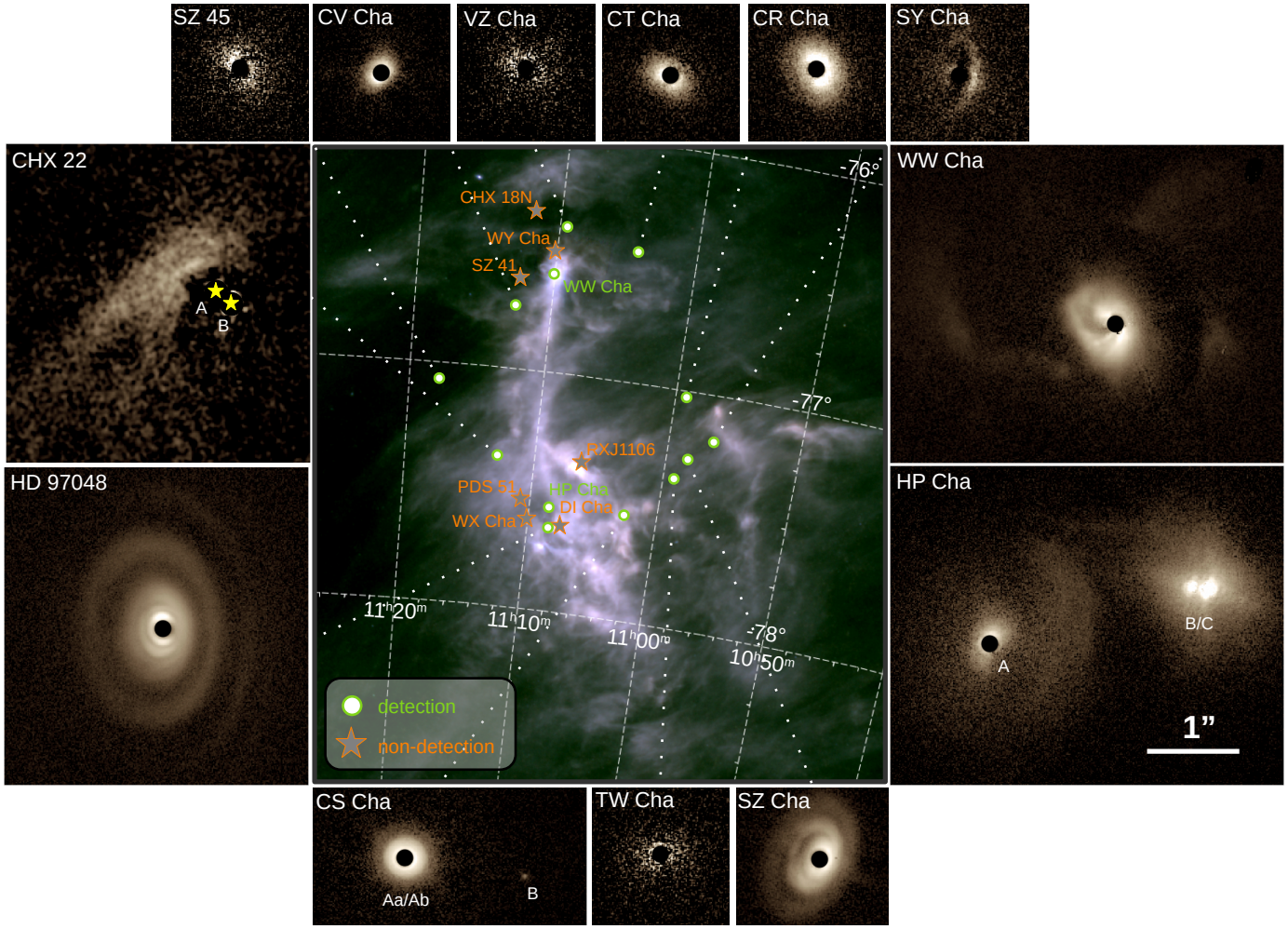

Fig. 2: Herschel/SPIRE RGB image of the Cha I star forming region constructed from the 150μm, 250μm and 500μm channels showing the interstellar dust (central panel). SPHERE/IRDIS Q_ϕ images for all systems with extended circumstellar dust in our sample (surrounding panels). The shown SPHERE data was taken in the H-band, with the exceptions of the HD 97048 and SY Cha system, for which we show K-band data, as well as the CS Cha system for which we show J-band data. We indicate the position of each detected source within the Cha I cloud with white markers with green boarder. We additionally show the positions of systems in our sample with non-detections of circumstellar dust with grey stars with orange borders. For the CS Cha, HP Cha and CHX 22 systems we indicate the position of visible stellar multiple components.

4.2.2. Sample aspect ratio

Using the fitting procedure described in section 4.2.1, we calculated disk aspect ratios for 11 systems in our sample. However, we note that the aspect ratios for 6 of these systems (CR Cha, CS Cha, SY Cha, SZ 45, TW Cha, VZ Cha) have large uncertainties (see table 3 for the disk height). We are plotting all measurements in figure 3 together with aspect ratio profiles from the literature for the extreme flaring Herbig star HD 97048 (Ginski et al. 2016) and for a sample of T Tauri stars (Avenhaus et al. 2018).

Within our sample we have two disks with multiple ringed structures, HD 97048 and SZ Cha. The disk around HD 97048 is by far the most extended reaching out to ~285 au. In this work we present new K-band measurements of this systems. Compared to the J-band measurements from Ginski et al. (2016) we find at all separation lower aspect ratios. This is an expected effect due to the lower dust opacity at longer wavelengths. We note that the slope between 45 au and 165 au for the system is well consistent with the slope derived from the J-band observation. Similarly we also find that for large separations the retrieved aspect ratio is no longer consistent with a single power law, likely due to a drop in dust surface density. For the SZ Cha system we measure the aspect ratio in two individual rings. Our results indicate that this disk shows the most extreme aspecdt ratio within our sample with values of XX and YY at ~59 au and 113 au, respectively. This is a much larger aspect ratio than found for either the HD 97048 system or for the average sample of T Tauri stars from Avenhaus et al. (2018).[2] The slope of the aspect ratio profile of SZ Cha is well consistent with the slope seen for HD 97048.

We find meaningful individual measurements of the disk aspect ratio for the CT Cha, CV Cha and WW Cha systems. Of these WW Cha is well consistent with the average profile of T Tauri stars from Avenhaus et al. (2018), while the disk around CT Cha appears flatter. The disk around CV Cha shows a higher

[2] We note that while we get very consistent results for both stages of our fitting approach for the inner ring at 59 au, we do see roughly a factor 2 increase in the aspect ratio for the outer ring and the constrained annulus grid method.

Table 3: Ellipse fitting results and system geometry from literature. In addition to inclination and position angle we give the amount (Δu) and angle (α_u) of offset of the fitted ellipse center from the stellar position. We give the height of the disk at the radius of the fit only taking the offset component into account that is in the direction of the disk semi-minor axis. Note that for the HD 97048 and SZ Cha systems multiple rings were fit independent of each other. In the *fit* column we indicate if the fit was performed based on the SPHERE data alone (*SPHERE*), using the SPHERE data but with inclination constrained to within 2° of the ALMA value (*SHERE/con*) or if its based on ALMA (literature) data (*ALMA*).

System	fit	i (°)	PA (°)	r (au)	Δu (mas)	α_u (°)	h (au)	ref.
CR Cha	SPHERE	34.9 ± 5.9	29.8 ± 14.0	93.6 ± 4.1	23.2 ± 17.9	237.9	-2.7 ± 9.6	this work
	SPHERE/con	31.0 ± 1.4	36.2	93.1 ± 4.2	0.0 ± 15.9	-	0.0 ± 5.7	this work
	ALMA	31.0±1.4	36.2±1.8	-	-	-	-	Kim et al. (2020)
CS Cha	SPHERE	21.6 ± 6.4	257.7 ± 31.1	84.9 ± 10.8	6.3 ± 14.0	316.0	2.7 ± 8.4	this work
	SPHERE/con	17.9 ± 0.1	82.6	85.4 ± 5.3	3.7 ± 14.7	-	2.3 ± 9.1	this work
	ALMA	$17.86^{+0.05}_{-0.01}$	262.6	-	-	-	-	Kurtovic et al. (2022)
CT Cha	SPHERE	45.7 ± 5.0	59.0 ± 9.4	64.6 ± 3.9	33.0 ± 17.2	133.3	8.3 ± 6.5	this work
	SPHERE/con	45.7 ± 5.0	59.0	64.6 ± 4.2	27.0 ± 19.6	-	7.2 ± 5.2	this work
CV Cha	SPHERE	43.0 ± 5.3	-46.7 ± 9.5	70.6 ± 4.0	42.6 ± 16.3	42.3	12.0 ± 6.2	this work
	SPHERE/con	43.0 ± 5.3	-46.7	71.1 ± 4.6	52.7 ± 12.3	-	14.8 ± 3.7	this work
HD97048	SPHERE	31.8 ± 7.1	-1.1 ± 15.7	45.4 ± 2.0	17.5 ± 10.4	119.9	5.3 ± 3.4	this work
	SPHERE/con	41.1 ± 0.9	4.5	45.4 ± 1.9	8.6 ± 1.2	-	2.4 ± 0.3	this work
	SPHERE	42.8 ± 3.5	2.3 ± 6.4	164.8 ± 6.4	129.2 ± 21.7	92.4	34.8 ± 11.0	this work
	SPHERE/con	41.1 ± 0.9	4.5	164.6 ± 6.3	125.1 ± 12.3	-	35.1 ± 3.5	this work
	SPHERE	47.1 ± 5.0	-4.8 ± 4.0	285.1 ± 11.9	142.3 ± 88.5	298.2	27.3 ± 146.4	this work
	SPHERE/con	41.1 ± 0.9	4.5	285.1 ± 11.7	196.2 ± 45.4	-	55.0 ± 12.8	this work
	ALMA	41.1±0.9	4.5±0.1		-	-	-	van der Plas et al. (2017a
SY Cha	SPHERE	60.4 ± 4.9	-8.7 ± 4.7	72.5 ± 6.6	43.7 ± 30.6	23.1	7.0 ± 15.5	this work
	SPHERE/con	51.7 ± 1.2	344.7	72.6 ± 6.6	51.5 ± 41.7	-	11.9 ± 9.6	this work
	ALMA	51.7±1.2	344.7±1.7	-	-	-	-	Orihara et al. (2023)
Sz 45	SPHERE	49.6 ± 5.8	215.0 ± 11.6	58.6 ± 3.3	26.3 ± 20.0	312.1	5.8 ± 8.3	this work
SZ Cha	SPHERE	46.8 ± 3.3	-22.9 ± 4.9	112.5 ± 4.9	91.4 ± 14.6	76.1	23.6 ± 4.8	this work
	SPHERE/con	42.1 ± 0.5	336.7	112.5 ± 4.7	147.0 ± 2.5	-	41.7 ± 0.8	this work
	SPHERE	38.8 ± 5.8	-11.5 ± 10.2	59.2 ± 3.1	64.3 ± 12.4	46.4	16.2 ± 5.2	this work
	SPHERE/con	42.1 ± 0.5	336.7	59.2 ± 3.1	61.3 ± 1.2	-	17.4 ± 0.4	this work
	ALMA	42.1±0.5	156.7±0.6	-	-	-	-	Hagelberg et al., in prep.
TW Cha	SPHERE	37.3 ± 9.0	-73.4 ± 34.6	35.4 ± 3.1	29.4 ± 20.0	124.8	0.2 ± 16.3	this work
VZ Cha	SPHERE	49.6 ± 5.1	55.7 ± 11.5	56.7 ± 3.4	46.3 ± 19.2	52.2	1.7 ± 9.8	this work
WW Cha	SPHERE	44.1 ± 3.3	29.8 ± 4.8	138.9 ± 5.2	65.6 ± 16.4	119.5	17.8 ± 6.0	this work
	SPHERE/con	36.2 ± 1	34.0	138.1 ± 4.9	77.2 ± 20.8	-	24.7 ± 6.7	this work
	ALMA	36.2	34.0	-	-	-	-	Kanagawa et al. (2021)

aspect ratio than expected from the literature profiles. There is considerable overlap within the uncertainties for all three systems, so it is not clear if they follow intrinsically similar aspect ratio profiles or if they are significantly different from one another. We note that as shown in appendix C, our edge-tracing approach to constrain the disk aspect ratio shows a systematic negative offset of ~0.05. If we consider this offset then the CV Cha system becomes consistent with the measurement for the extremely flaring SZ Cha system, while WW Cha would be consistent with the profile for the HD 97048 system.

Generally we find that all disks with well constrained aspect ratios show values larger than 0.15 at separations past 50 au (including the bias correction of the measurement method). Conversely we find that for the sample of disks with large uncertainties in their recovered aspect ratios (grey and black data points in figure 3), the general trend is that they have low aspect ratios. Within this sub-sample the CS Cha system is a special case. Since it is seen under very low inclination (~20°) the result of our edge-tracing fitting approach is intrinsically very uncertain. So it may well be that the system exhibits a larger aspect ratio than what we recover. However the remaining 5 systems with large uncertainties (CR Cha, SY Cha, SZ 45, TW Cha, VZ Cha), are all seen under intermediate inclinations. In all of these cases the large uncertainties originate in the comparatively low signal to noise ratio of these disk detections. As well will discuss in section 4.3 this low SNR is linked to the intrinsic faintness of these disks relative to their central star.

4.3. Disk polarized scattered light contrast

The scattered-light brightness of a disk is not immediately assessed from the image. In fact, several elements contribute to the amount of detectable NIR flux (stellar luminosity, self-shadowing, disk geometry, scattering phase function). To alleviate this degeneracy, here we calculate the polarized contrast[3] of our sources as in Garufi et al. (2014, 2017). This method consists of dividing the observed polarized flux at a certain location by the net stellar flux that is virtually incident on that disk region (that is the stellar flux diluted by the distance). Also, the measurement is performed along the major axis (approximately 90° scattering) to minimize the dependence on the scattering phase

[3] We note that polarized contrast might be a somewhat misleading term. We use it here for consistency with previous studies. What we in fact calculate is effectively an albedo of the disk at the observed wavelength.

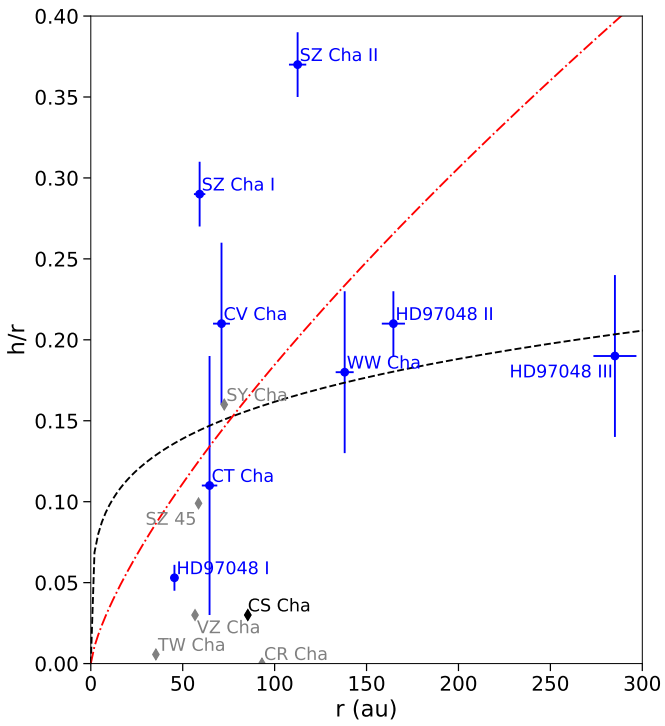

Fig. 3: Aspect ratio for all disks with at least one measured surface height. The black dashed line is the fit to several T Tauri stars done by Avenhaus et al. (2018), while the red dash-dotted line is the fit to the HD 97048 Herbig star, located near Cha I, from Ginski et al. (2016). Data points in grey and black have intrinsically very large uncertainties (not displayed).

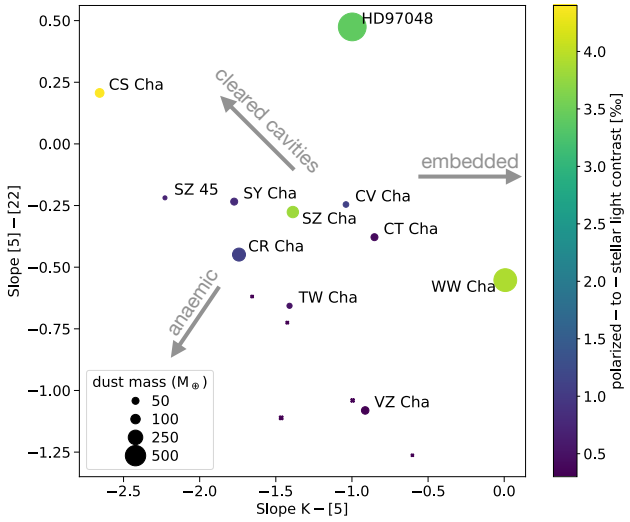

Fig. 4: Slopes of the target SEDs between K-band and 5 μm as well as 5 μm and 22 μm. The polarized-to-stellar contrast is given by the color bar. Also the size of symbols scale with the contrast ratio.

function. Finally, a unique number is obtained for each disk by averaging the values obtained over the separations with detected flux.

In Figure 4 we plot the obtained polarized contrast versus the near (2.2 μm to 5 μm) and mid-infrared (5 μm to 22 μm) SED slopes for each system. A reversal in the sign from a negative near-infrared slope to a positive mid-infrared slope indicates classical transition disks, which show a lack of flux typically around 10 μm, due to a cavity in the disk. In our target sample, only CS Cha and HD 97048 are such classical transition disks. CS Cha shows by far the most prominent flip between near and mid-infrared slopes. At the same time it is also clearly the brightest disk in scattered light. HD 97048 equally appears bright in scattered light, though not as extreme as CS Cha. Its shallower near infrared slope indicates the presence of some near infrared excess emission and thus some disk material close to the central star.

The only other comparably bright sources within our sample are WW Cha and SZ Cha. WW Cha shows a near flat near infrared slope indicative of the star still being heavily embedded. In figure 16 we see that the disk is indeed still surrounded by either primordial cloud material, or material ejected from the system. The position of SZ Cha in figure 4 is somewhat puzzling. Both its near and mid-infrared slope are average among our sample, indicating that dust is present in the inner and outer system. Yet despite it showing similar SED slopes than several other disks it is significantly brighter, i.e. more compareable to the transition disk HD 97048. This is likely connected to the extreme flaring that we find for the disk in section 4.2.

In general, Figure 4 shows a trend that disks appear fainter in scattered light if they have steep mid-infrared slopes (< -0.25). In particular all our faint non-detections have a mid-infrared SED slope smaller than -0.5. Systems with a comparable near and mid-infrared slope can be considered full disks, without large cavities. There may be a trend that disks appear brighter in the upper left quadrant and fainter in the lower right quadrant. Thus as the 'transitional' character of the disk becomes stronger it also increases in scattered light brightness, consistent with the view that removal of material close to the central star leads to less self shadowing of the outer disk. This is very similar in nature to the finding of Garufi et al. (2018) who studied disks around Herbig stars in scattered light. They found that there is a clear trend for Group I Herbig stars (as defined by Meeus et al. 2001) to be brighter than Group II Herbig stars. Group I is differentiated from group II by the presence of a strong far infrared excess in the SED, indicating the presence of a cold dust component. Garufi et al. (2018) show that a high far to mid-infrared flux ratio correlates with increase brightness in scattered light.

To understand how the scattered light brightness might depend on other system parameters, we show in Figure 5 the polarized contrast plotted versus the system dust mass, the disk-mass normalized accretion rate and the system age. In particular the polarized contrast seems to increase with dust mass. Conversely we did not detect scattered light signal from disks with dust masses lower than 10 $M_\oplus$. To quantify this trend we calculated the Kendall τ-coefficient (Kendall 1938). We find a correlation with τ_K=0.58 and a probability of 1.6 % that both quantities are unrelated. We note that this correlation of the dust mass and the polarized contrast could be influenced by the fact that we used ALMA band 7 fluxes to obtain dust mass estimates. However, as recently discussed by Ballering & Eisner (2019) and Ribas et al. (2020) the disk may well be partially optically thick in band 7 and the measured fluxes may depend not just on dust mass and temperature but also the viewing geometry.
For the normalized accretion rate a possible weak correlation between low accretion rates and high polarized contrast is visible. However, CR Cha and SY Cha seem to not follow this trend, i.e. they have very low accretion rates compared to their dust mass, yet they are significantly fainter in scattered light than CS Cha, SZ Cha and WW Cha, which have all higher accretion rates.

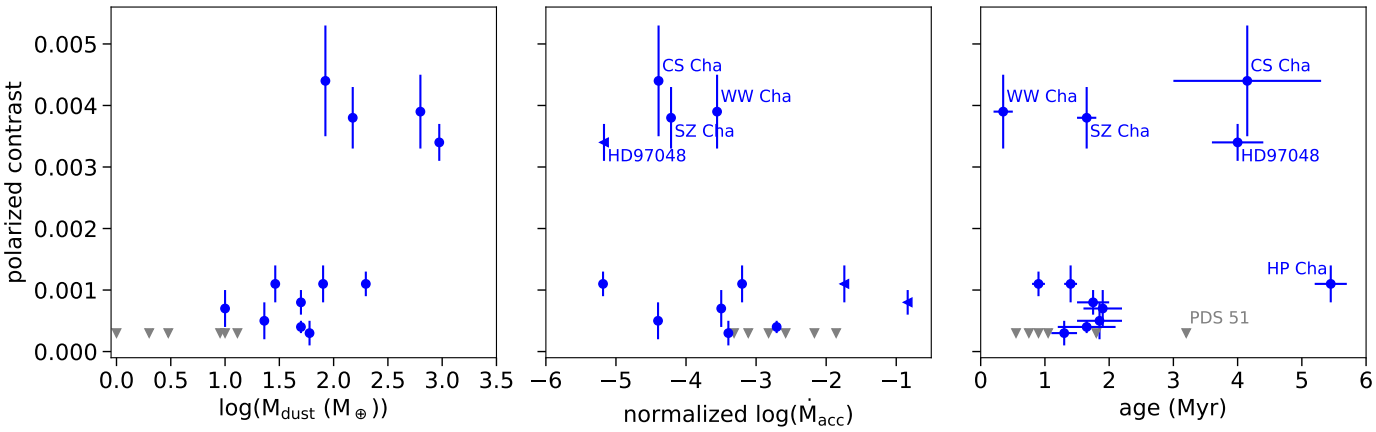

Fig. 5: *Left:* Polarized contrast versus dust mass in the system as measured from ALMA continuum photometry. *Middle:* Polarized contrast versus accretion rate of the systems as measured by Manara et al. (2019), normalized by the dust mass in each system. *Right:* Polarized contrast versus system age.

Finally we do not recover a clear correlation between system age and polarized contrast. However, it is noteworthy that out of the group of faint or non-detected disks all but two are younger than 2 Myr. The outliers are PDS 51, which has the lowest detected dust mass in our sample (2 $M_\oplus$) and HP Cha which is an interacting triple systems (Zhang et al. 2023). Conversely the disks around CS Cha and HD 97048 are the brightest objects in our sample and with the exception of HP Cha also the oldest. For the bright disks WW Cha and SZ Cha are not following this potential age-polarized contrast relation. For WW Cha this may be related to the strong interaction of the system with the surrounding cloud.

5. Results on individual systems

The thirteen detections of our sample are very diverse. CHX 22 and HP Cha clearly reveals some evidence of interaction between che companions. As described in Zhang et al. (2023), the image of CHX 22 reveals a tail-like structure that surrounds the close binary. The very low disk mass in dust revealed by the ALMA images ($< 1 M_\oplus$, see Sect. 2) points to a very small disk that is clearly shaped by the presence of the companion. Instead, the individual stars of the HP Cha are clearly more separated, and the primary disk is likely less disturbed by the companion even though a tenuous streamer indicates that an interaction between the two component is in place (Zhang et al. 2023).

The disk of HD97048 is evidently the most extended disk of the sample, as well as of one of the most prominent disk detections in the entire literature. As described by Ginski et al. (2016), alternating rings and gaps are detected from 40 au to 340 au from the star. Conversely, the disk of Sz45 and TW Cha are faint and apparently featureless in scattered light (see Garufi et al. 2020, 2022, respectively). Their faintness is most likely due to a self-shadowed geometry where the disk inner region intercepts and reprocesses a large fraction of the stellar photons (Dullemond & Dominik 2004; Garufi et al. 2022).

Hereafter, we focus on the eight sources presenting features that are relevant for this work. These are: CR, CS, CT, CV, SY, SZ, VZ, and WW Cha. Subsequently, we discuss the seven non-detections of the sample.

5.1. CR Cha

We detect a smooth and featureless disk around CR Cha. In the non-coronagraphic images we find clear signal down to 85.6 mas with no indication of a resolved inner cavity. This is consistent with recent ALMA observations by Kim et al. (2020), who do likewise not recover a cavity in dust continuum emission or gas emission at similar spatial scales. In the deep coronagraphic images we find signal out to 0.6″ (112.5 au) along the disk major axis. This includes the region at 90 au, where there is a clear detection of a gap and a narrow outer ring in the ALMA dust continuum. We do not find significant evidence for this gap in scattered light, but caution that the signal-to-noise of our data is low beyond ~0.4″ (79 au). In figure 6 we show that the radial profile along the major axis is dropping consistent with the r^{-2} illumination effect. It is thus possible that a longer observation will detect scattered light signal at larger separations. Indeed CO gas is detected with ALMA out to 240 au (1.28″, Kim et al. 2020).
The disk shows a strong brightness asymmetry between the North-West and the South-East side, expected from phase function effects in scattered light. The North-West side is significantly brighter than the South-West, from which we conclude that the North-West side is the near side of the disk, showing strong forward scattering.

5.2. CS Cha

The circumstellar disk around CS Cha was first resolved in Ginski et al. (2018) in the J and H-band in polarized light. We have now added polarimetric observations with SPHERE/IRDIS in the K-band and with SPHERE/ZIMPOL in the R and I-band. The disk is detected in all bands, shown in figure 7. We also show the extracted profiles along the major axis in figure 8.
Based on ellipse fitting in scattered light the disk has an inclination of 24.2°±3.1° and a position angle of 284.4*degree* ± 2.2°. We used available high spatial resolution (beam size 0.09″ × 0.06″) ALMA continuum Band 7 data (Kurtovic et al. 2022) to test the inclination and position angle. A MCMC fit of a ring model to the visibilities finds broadly consistent values of $17.86° + 0.05_{-0.01}$ for the inclination and 262.6° for the position angle. Since the ALMA data is not affected by illumination and

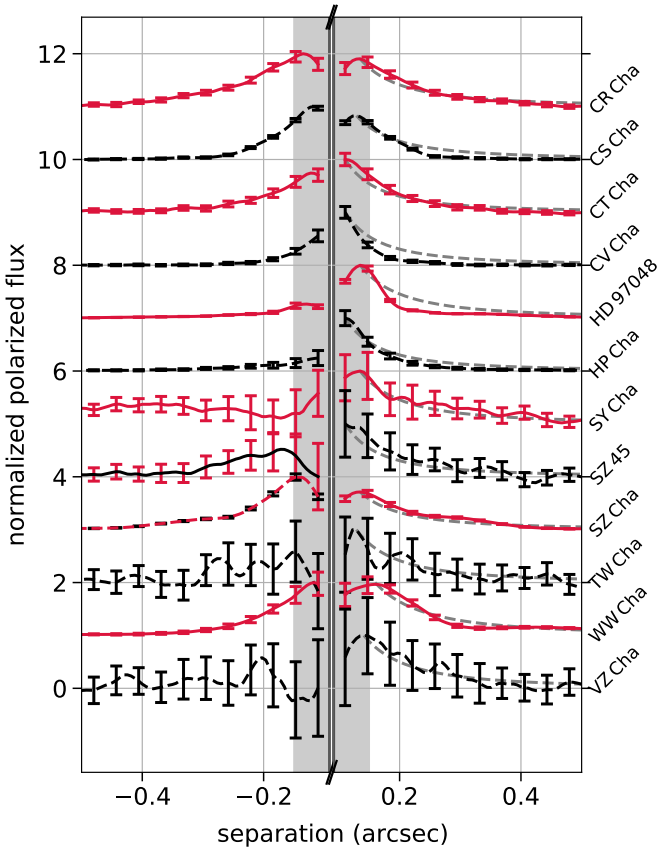

Fig. 6: Radial profiles of all detected disks along the major axis. The polarized flux is in all cases normalized to unity. The profiles of individual disks have been vertically offset from each other for better readability. The region directly covered by the IRDIS coronagraph is excluded from the plot, while the region that is still influenced by coronagraph suppression is shaded light grey. Grey dashed lines are added on the right side of the plot to indicate a r^{-2} drop-off, expected from a scattered light signal.

phase function effects we adopt the ALMA values for further analysis.

As is visible in figure 8, the disk around CS Cha appears smooth in all bands without distinct morpohological features (we omit the R-band in this figure due to its low SNR). We do not resolve the inner cavity (seen in ALMA data and inferred from the SED) in scattered light down to the inner working angle of the employed coronagraphs, i.e. 92.5 mas for IRDIS and 77.5 mas for ZIMPOL. In figure 6 we show the radial profile of the disk along the major axis in J-band compared to a r^{-2} illumination drop-off. Between 0.20″and 0.25″the profiles drops off more steeply than the expected illumination function. This is an indication that either the farther out regions of the disk are strongly shadowed, or that the disk is sharply truncated at 0.25″ (44 au).

From the different observation epochs of CS Cha we extracted flux calibrated brightness profiles measured as contrast to the star in circular apertures along the major axis of the disk. Since the R-band data is a low signal-to-noise detection we excluded it from this analysis. The profiles are shown in figure 7.

The disk profiles show a near identical slope and contrast in the J and K-band, while the disk appears slightly fainter in the H-band. In the optical I-band the disk is significantly fainter than in the near infrared. The deviation of the H-band from the near grey scattering in the J and K-band is somewhat surprising. We however caution that the H-band data is of significantly worse quality than the J and K-band data due to the low atmosphere coherence time during the observation (see table A.1). In particular the coherence time degraded between start and end of the observation, while flux calibration frames were only taken at the end of the observing sequence. This may have introduced a systematic effect in the photometric calibration of this data set, as was already discussed for the same data in Ginski et al. (2018). However, we would expect such an effect to lead to an over-prediction of the disk brightness rather than an under-prediction[4].

5.2.1. CS Cha: Scattered light color analysis

To investigate the dust properties at the scattering surface of the disk we computed the integrated polarized scattered light in an annulus between 0.09" and 1.0" for the IRDIS, near-infrared images. The inner radius was chosen to exclude the region covered by the coronagraphic mask, while the outer region was selected such that all disk flux is included. We then computed the brightness ratio of polarized scattered light to stellar total intensity, as measured in the flux calibration frames of each epoch. We find very similar flux ratios of 4.3×10^{-3} and 4.6×10^{-3} for the J and K-band respectively. As already expected from the disk profiles, we find a lower ratio of 2.4×10^{-3} for the H-band. For the ZIMPOL R and I-band data we measured the integrated polarized scattered light in an annulus between 0.07" and 1.0", taking into account the smaller coronagraph size. We find flux ratios of 1.0×10^{-3} and 1.7×10^{-3} for the two bands respectively.

Ignoring the H-band data, which may suffer from calibration issues discussed in detail in Ginski et al. (2018), we find that the scattered light shows near grey color between the J and the K-band, while the polarized scattered light flux drops sharply between the J and the I-band. To model this we used the radiative transfer code RADMC3d (Dullemond et al. 2012). We assumed compact spherical grains made of pyroxene silicate (refractive index taken from), with a size distribution with a minimum grain size of $0.1\mu m$ and a power law index of -3.5. The maximum grain size a_{max} was left as a free parameter. Optical properties were computed using the Mie theory by utilizing the public code *Optool* (Dominik et al. 2021). We used the inclination of CS Cha of ∼22°, as measured from the ALMA data with a small flaring exponent of 1.09, to adjust the overall disk brightness to our observations. The remaining model parameters are identical to the ones presented in Tazaki et al. (2019). We show the resulting integrated flux ratios in figure 9 and the corresponding synthetic images in figure E.1.

For compact grains, the degree of linear polarization drops rapidly once the size parameter ($x = 2\pi a/\lambda$, wherein a is the grain radius) exceeds unity. This explains why the integrated polarized flux decreases for shorter wavelengths for all models. However, the wavelength at which the polarized flux drops depends on the grain radius. The observations suggest this happens between the I and J bands. From model calculations, we found that a model with $a_{max} = 0.32\mu m$ successfully reproduces the steep decline in polarized flux between I and J bands. The presence of such small grains is also in harmony with the lack of brightness asymmetry, i.e., forward scattering, in the observed images at near-IR wavelengths shown in figure 7. However, we note that model predicts a slightly blue J-K color, while our ob-

[4] The AO system produced a worse correction for the flux calibration frames than for the disk science data, making the star effectively appear fainter relative to the disk

servations found a slightly red color. A large exploration of the parameter space may be necessary to fully reconcile our observations with the radiative transfer models, which is outside of the scope of this study.

5.2.2. CS Cha: Stellar binary

The ZIMPOL observation sequences in R and I-band of the system included short non-coronagraphic sequences for flux calibration purposes. In these sequences we found that the primary star in the system is for the first time resolved as visual binary star (figure 10). CS Cha A was already known to be a spectroscopic binary from radial velocity observations taken by Guenther et al. (2007). They found that the system may have a mass ratio close to 1 and an orbital period of or longer than 2482 days. However, since they did not cover a full orbit they could not further constrain the orbital parameters. Our ZIMPOL observation finds a flux ratio of 0.31±0.03 in R-band and 0.41±0.02 in I-band. To convert the flux ratio to apparent magnitudes we use the cataloged I-band magnitude of 10.12±0.04 mag (Kiraga 2012) and the R-band magnitude of 10.7±0.3 mag (Smart & Nicastro 2014). Since the binary was unresolved for these measurements we corrected the primary star magnitude following Bohn et al. (2020), using the flux ratio between the two components as input. This yielded a corrected I-band and R-band magnitudes of the primary star of 10.49±0.04 mag and 11.0±0.3 mag respectively. Given our measured flux ratio, the secondary then has apparent I and R-band magnitudes of 11.46±0.06 mag and 12.3±0.3 mag, respectively. Assuming a system age of $7.6^{+1.6}_{-1.3}$ Myr and BT-SETTL model isochrones (Baraffe et al. 2015b), we find masses of 1.17 $M_\odot$ and 0.8 $M_\odot$ for Aa and Ab, with a typical uncertainty of 0.02 $M_\odot$ based on the age and photometric uncertainty. This uncertainty may be underestimated, given that different isochrone models may well yield slightly different results.
To extract the astrometry from the ZIMPOL images we simultaneously fitted two Moffat functions to the binary star. A Moffat function is typically a very good fit to the ZIMPOL point spread function (PSF), especially for fainter stars, since it still has a significant seeing limited halo surrounding the diffraction limitted PSF core. We find a separation of 31.6±1.3 mas at a position angle of 297.7°±2.1°. The astrometric calibration of the detector was derived from several visual binary stars with well known orbits as well as the internal pin-hole calibration grid (Ginski et al, in prep.).
We combined the radial velocity measurements given by Guenther et al. (2007) with our new astrometric measurement to derive the orbit of the CS Cha Aab pair. We use the *orbitize!* python package for the fit with the included Markov-Chain Monte-Carlo sampler (Blunt et al. 2020; Foreman-Mackey et al. 2013). We set the prior of the combined system mass using a Gaussian distribution with the peak at 2.35 $M_\odot$ and the standard deviation of 0.5 $M_\odot$. We ran 1.2×10^6 orbit solution with 50 walkers. The results for the semi-major axis, the eccentricity and the inclination of the orbit are displayed in figure F.2.
The resulting distribution roughly shows two distinct orbit families, either low-inclination pro- or retrograde orbits, or strongly inclined orbits peaking at ~80°. The first orbit family is roughly consistent with the binary orbit lying in the plane of the circumbinary disk, while the second orbit family is roughly perpendicular to the disk plane. In both orbit families we find a range of possible eccentricities with a peak in the distribution at a value of ~0.25. The semi-major axis peaks at ~7.5 au for the low-inclination orbits and at ~15 au for the highly inclined orbits. To illustrate the size of the orbit relative to the detected sub-mm continuum gap in the disk (Francis & van der Marel 2020), we show several orbits over-plotted with the ZIMPOL and ALMA data in figure 11.
Given our orbit solutions it is interesting to investigate if the binary companion can be solely responsible for opening the gap in the disk traced by the ALMA data. The cavity radius from ALMA found by Francis & van der Marel (2020) and scaled to the new Gaia EDR3 distance is 35.5 au. The mass parameter $\mu = M_2/(M_1 + M_2)$ for the CS Cha system is 0.41. The calculations by Artymowicz & Lubow (1994) indicate that for an eccentric binary system with $e = 0.25$ (identical to the peak we find in the orbit distribution for CS Cha) and a slightly lower mass companion with $\mu = 0.3$, the outer edge of the cavity should be located at $2.6a$. Given the range of semi-major axes recovered by our orbit fit that is a range of 19.5 au up to 39 au. Given that in our case the binary component has an even larger fraction of the total system mass, this range should still shift slightly to larger outer gap radii. This range is then well consistent with the cavity radius found by ALMA, and thus it may be possible in principle that the disk cavity can be explained by the binary companion. However, we note that Kurtovic et al., subm. argue that based on the brightness asymmetry observed in the ALMA data (not discussed in our study), an additional planet might be needed to explain the uneven distribution of material in the ring.

5.3. CT Cha

We find a compact smooth disk around CT Cha A. With fitting of the scattered light data as described in section **??** we find that the disk major axis goes from the North-East to the South-West (see table 3). The disk shows a high inclination of 45.8°±1.0°. The disk profile drops with the expected r^{-2} illumination effect and is detected out to 0.35″. Since the disk signal drops at the rate expected due to central illumination it is well possible that the disk extends beyond this range. Evidence for this is that we do not detect signal from the forward scattering peak of the backside of the disk, as is seen in other highly inclined systems (e.g. IM Lup, DoAr 25, IK Lup Avenhaus et al. 2018; Garufi et al. 2020). Such signal would be blocked from view if the disk indeed extends to larger radii.
As expected from the polarized scattering phase function we receive strong signal from the disk ansae where scattering angles are close to 90°. We detect the disk to slightly larger separation along the minor axis in the South-East than in the North-West. For a strongly inclined disk this is expect due to the bowl shape of the disk surface if the North-West side is the near side of the disk, which mainly shows a very narrow forward scattering rim. The peaks of the phase function are moved from the ansae in direction of the minor axis on the South-East side. This is again expected if we observe a flaring disk with the far side in the South-East and the near side in the North-West (e.g., de Boer et al. 2016).
We note that we detect unresolved polarized light originating from the known substellar companion CT Cha b. This object is discussed in detail in Schmidt et al., in prep., including the polarimetric data presented here.

5.4. CV Cha

We resolve a bright, compact disk around CV Cha. In the non-coronagraphic images of the system significant signal is detected down to 0.05″ (9.5 au). We do not resolve a cavity in scattered

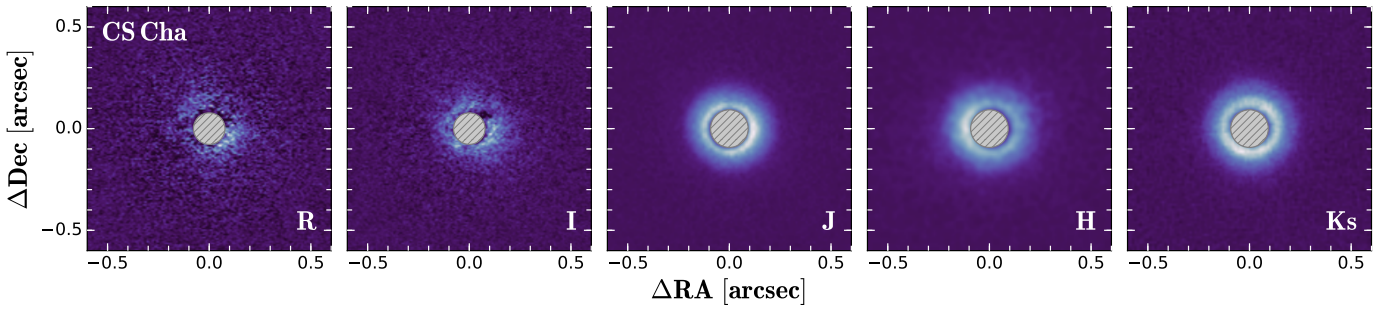

Fig. 7: Multi-band polarimetric observations of the disk around the CS Cha system with SPHERE/ZIMPOL and SPHERE/IRDIS. The filter band is indicated in each image. Displayed are the Q_*phi* images for all bands. The grey hashed disk in the center marks the size of the coronagraphic mask that was employed.

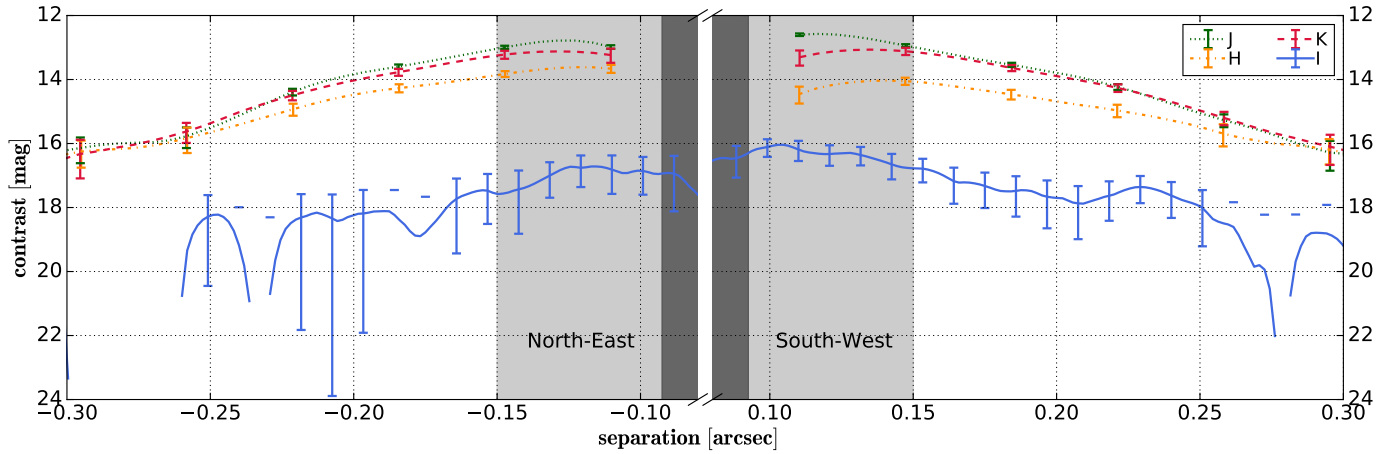

Fig. 8: Radial contrast profiles of the CS Cha multi-band observations along the major axis. The contrast is calculated relative to the total intensity of the central star. Filter band is indicated by line style and color. The region covered by the utilized coronagraphs is shaded dark grey, while the region where coronagraph suppression is still significant is shaded light grey. Note that the ZIMPOL coronagraph is smaller than the IRDIS coronagraph such that the I-band data can be traced further in. Due to the noisy nature of the R-band data it is excluded here.

light. Ellipse fitting of the scattered light data finds the major axis from the South-East to the North-West. The disk appears similarly strong inclined as the CT Cha system with a recovered inclination of 43.8°±0.3°. However, different from the CT Cha system the radial profile along the major axis drops of much steeper than expected from illumination effects (see figure 6). This indicates that the disk is either indeed small or strongly self shadowed beyond the point where we detect it. As was the case for CT Cha we do not detect the backside of the disk, which may indeed indicate that the disk extends further and blocks our line of sight to the backside. This may indicate that the region we observe is strongly puffed up and casts a shadow on the outer disk regions. The disk was not resolved in Pascucci et al. (2016) in ALMA mm continuum emission with a beam size of 0.7″×0.5″, in agreement with our observations tracing smaller grains. However the gas could extend much further and only small surface densities of μm dust grains are needed mixed in the gas to make the extended disk optically thick in the near infrared. Thus an extended gas disk with a high gas-to-dust ratio might fit well with our observations.

The disk is detected at larger separations along the minor axis towards the North-East. Similar as for CT Cha we interpret this as the far side of a flared, inclined disk.

We find two distinct dips in the azimuthal brightness distribution along the minor axis. We highlight these in figure 12. In principle it is expected that the polarized scattering phase function peaks in the ansae and produces less signal toward forward and back-scattering sides of the disk. However, in practice the forward scattering side of the disk is rarely much fainter than the ansea when it is indeed resolved (see e.g. the polarized phase function measured for the HD 97048 system, Ginski et al. 2016). Furthermore in figure 12 it is visible that in particular the dip on the forward scattering side of the disk is very sharp. If this were a phase function effect we would expect a smoother transition from bright to dark azimuthal areas. Such azimuthal brightness dips have now been observed in a number of systems, e.g. HD 142527 (Marino et al. 2015) or HD 100453 (Benisty et al. 2017), and are usually attributed to a misaligned inner disk casting a shadow on the resolved outer disk. To produce narrow shadows the misalignment has to be significant. The position of the dips along the minor axis indicate not only a misalignment in inclination but also in position angle of the inner disk. Optical interferometry or possibly the longest baseline ALMA observations may be able to resolve the inner disk zone and confirm such a misalignment.

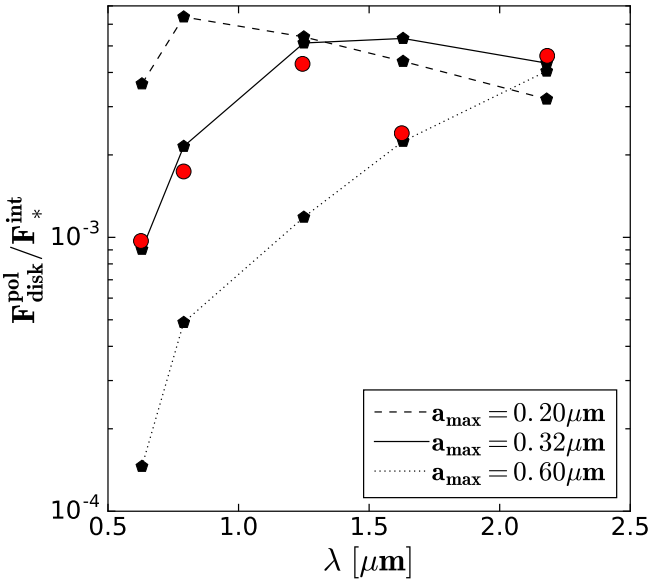

Fig. 9: Integrated polarized scattered light to total intensity stellar flux ratio for CS Cha (red dots). We note that the H-band data might suffer from systematic calibration issues as discussed in Ginski et al. (2018). We additionally show the same for different compact dust aggregate models computed for the inclination of the CS Cha system, assuming a settled disk with a flaring exponent of 1.09. Dust particles are spherical and we considered a size distribution with minimum grain size of $0.1\mu m$. The maximum grain size is a free parameter and indicated in the figure.

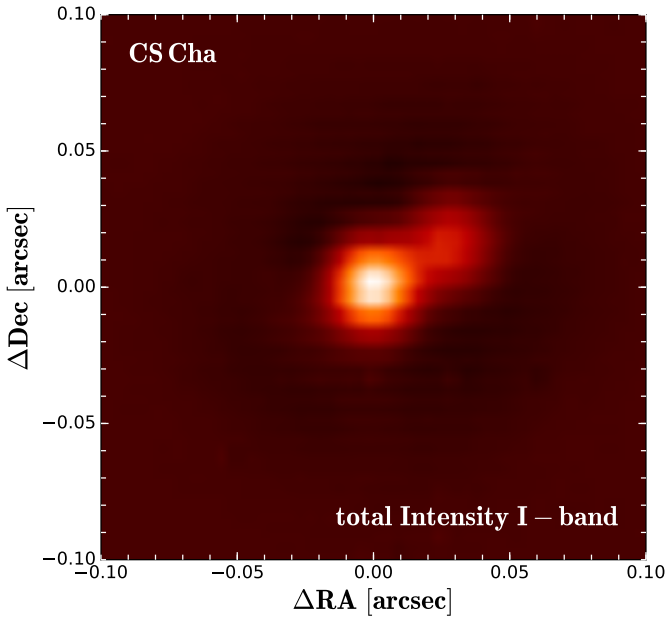

Fig. 10: SPHERE/ZIMPOL I-band observation of CS Cha A. The primary star is resolved in two components. The data is shown on a linear color scale.

5.5. HD 97048

The HD 97048 is a well studied Herbig star. Lagage et al. (2006) resolved the disk around this system for the first time in mid-infrared poly-cyclic aromatic hydrocarbon (PAH) emission and found that it is extended and strongly flaring. Subsequent scattered light observations with HST/ACS traced disk structures out to ~600 au (Doering et al. 2007). More recently the planet-forming disk was resolved with extreme adaptive optics observations in the near-infrared with VLT/SPHERE and Gemini/GPI in the J and H-band, respectively (Ginski et al. 2016; Rich et al. 2022). These observations revealed multiple rings and gaps at radial separations between 40 au and 340 au. Ginski et al. (2016) extracted the height profile of the disk by tracing the center offset of rings and gaps along the disk minor axis and found that the disk scattered light surface height profile can be described by a single power law with a large flaring exponent of 1.73 [5]. Complementary sub-mm observations of the system found a central cavity in the dust continuum emission with a size of 40-46 au (van der Plas et al. 2017b; Walsh et al. 2016). Using high spectral and spatial resolution ALMA gas line observations Pinte et al. (2019) reported the detection of dynamic signatures in the disk, consistent with the presence of an embedded gas-giant planet at an orbital separation of 130 au.

Within our survey we present new VLT/SPHERE K-band polarimetric observations of the system. We show the corresponding Q_ϕ image in figure 13. The new K-band data is of significantly higher signal-to-noise compared to the J-band observations presented in Ginski et al. (2016). In particular ring 3 (at ~ 280 *au*) from Ginski et al. (2016), which they only detected in total intensity angular differential imaging reductions, is well recovered in the new K-band polarimetric image. As previously discussed

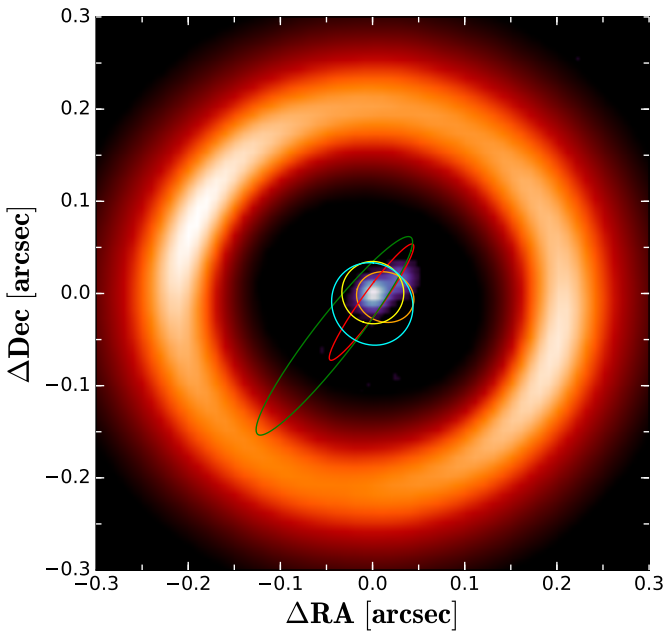

Fig. 11: Combined image showing the ALMA continuum observation at $887\mu m$ of CS Cha, first published by Francis & van der Marel (2020), together with the new ZIMPOL data showing the resolved stellar binary. We over-plot five random orbits from the resulting MCMC fit shown in figure F.2 to illustrate the size of the binary orbit relative to the cavity size in mm-continuum.

[5] We note that recently Rich et al. (2021) found an even larger flaring exponent after suggesting a different fitting approach for one of the disk rings in HD 97048.

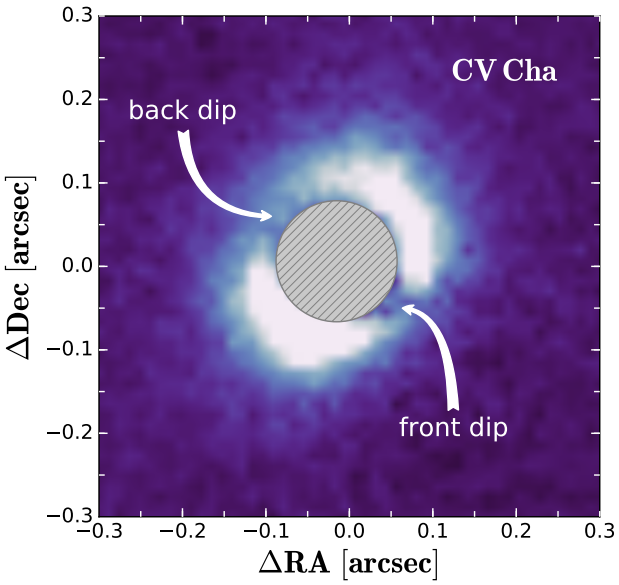

Fig. 12: Qϕ image of the CV Cha system from J-band observations. Two steep azimuthal dips in brightness are detected.

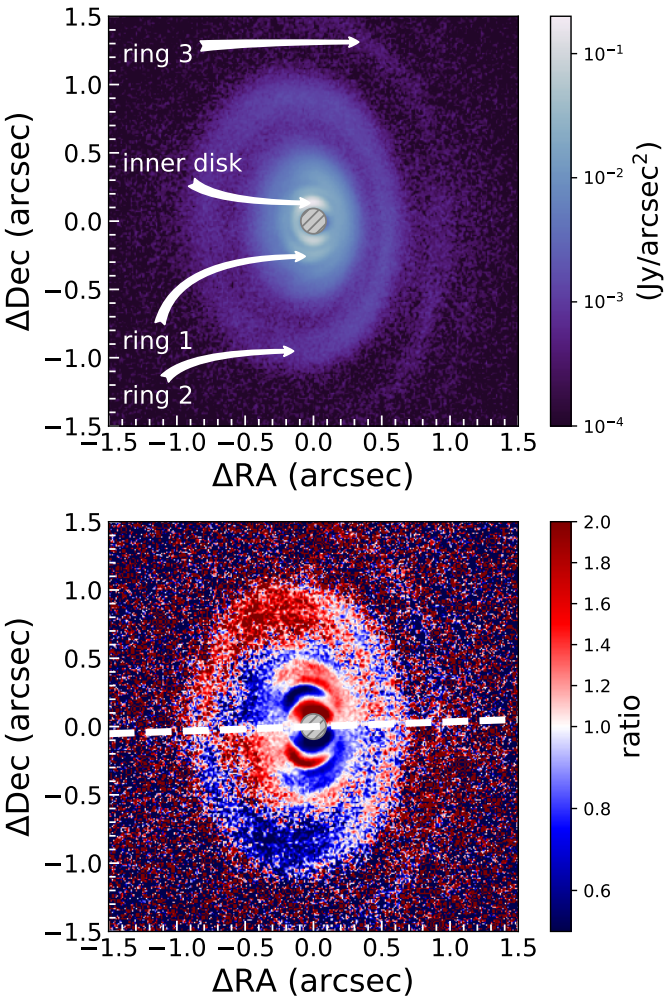

Fig. 13: Axial asymmetry of the disk surrounding HD 97048 relative to the minor axis from SPHERE K-band observations. We flipped the disk around its minor axis and then divided the original image by the flipped image. The ratio between the two is indicated by the color map. The white dashed line indicates the disk minor axis.

in section 4.2, we extracted the height profile of the disk from the K-band image and find a similar but overall lower profile as was recovered for the J-band data. This is consistent with the lower dust opacity in the K-band.

Due to the higher signal-to-noise of the new K-band data, we identify for the first time strong asymmetries in the disk scattered light image. We are highlighting these asymmetries in the bottom panel of figure 13. There we show the ratio of the disk surface brightness between the original image and an image flipped along the disk minor axis. For a perfectly symmetric disk, we would expect a ratio of 1, i.e. axis symmetry with respect to the disk minor axis. Instead for HD 97048 we find deviations of up to a factor of ∼2. Curiously we see a pattern along the disk major axis (from North to South in the image) where the disk surface brightness flips from rations smaller than 1 to ratios larger than 1. This brightness asymmetry can be well observed also in the top panel of figure 13. The inner disk appears brighter in the north, while ring 1 appears brighter in the south. A similar effect was observed for the multi-ringed disk around the T Tauri star RX J1615.3-3255 by de Boer et al. (2016). They argued that this may be caused by oscillating shadowing of the outer rings by the next innermost ring. However, they suggest that such shadowing should only be expected for disks with low flaring exponents, whereas the disk around HD 97048 is strongly flaring. Muro-Arena et al. (2020b) showed that small (few degrees) relative misalignments within the disk around HD 139614 can explain the large brightness asymmetries observed in this system. Following this logic the asymmetries observed in the HD 97048 system may be interpreted as small scale warps within the disk, which change alignment moving radially within the disk. This may be consistent with the evidence that at least one high-mass planet is embedded in the disk from Pinte et al. (2019). If the orbital plane of this planet is slightly misaligned with the disk plane, then the planet could be responsible for warping the disk, similar as is suggested for the much more evolved β Pic system (Dawson et al. 2011). Given the multiple "flips" in brightness asymmetry that we observe it may also be possible that this disk asymmetry is not static, but that we observe signs for a dynamic warp, which produces time dependent "ripples" within the disk.

5.6. SY Cha

We detect clear scattered light signal around SY Cha. However the shape of the signal appears complex and not easy to interpret. Some of the detected structures have low signal-to-noise, in part due to low data quality. The primary star in the SY Cha system is faint in the optical (Gmag = 12.53±0.01, Gaia Collaboration et al. 2018) and thus a challenging target for the adaptive optics system of SPHERE (see Jones et al. 2022). During the observation the tip-tilt stabilization had to be disabled, resulting in the star moving slightly behind the coronagraphic mask. While realignment of all frames was performed, using faint background stars as calibrators, this still resulted in degraded performance.

In figure 14 we see that signal was detected right outside of the coronagraphic mask with a strong peak in the West. In the same figure we show the ALMA Band 6 continuum data from Orihara et al. (submitted). In the ALMA data the disk is resolved into an

outer ring with an azimuthal asymmetry between the north-east and the south-west, an inner cavity and an unresolved inner disk component. The position angle of the major axis and the inclination were extracted from the ALMA data and are shown in table 3. The major axis is located at a position angle of ∼345°. This fits well with the SPHERE data which show extended signal along the North-South direction.

The inclination of the disk is ∼52° as measured from ALMA. In the left panel of figure 14 we overlay an ellipse with the ALMA inclination and position angle scaled to the scattered light features. The ellipse traces a low signal-to-noise structure, better visible in the West and somewhat visible in the East, which may be the scattered light counterpart of the ALMA ring. Due to the higher polarized intensity signal in the West we assume that the Western side is the near side of the disk.

To the North there is asymmetric structure outside of this ellipse which presents as a clump and a possible arc-like structure. Both of these asymmetric structures roughly coincide with the over-brightness in the ALMA Band 6 data as is best visible in figure 14, right panel. This asymmetry in ALMA continuum flux was already noted by Pascucci et al. (2016) in their lower resolution Band 7 data. In Band 7 the disk starts to become optically thick, thus the over-brightness could be either a temperature or a density effect. That the asymmetry is still present in the optically thinner Band 6 data may suggest that it is caused by an enhancement of material rather than an increase of temperature.

Scattered light is typically most sensitive to the scale height of the disk which in turn determines the $\tau = 1$ height of the scattering surface. Both, a dust (and gas) over-density or an increase in temperature may increase the scale height of the disk (see the case of SR 21 where both effects are visible in scattered light, Muro-Arena et al. 2020b). For a deep discussion of the ALMA Band 6 data we refer to Orihara et al. (submitted).

Given the low signal-to-noise of the the scattered light data, we can at this point only speculate on the origin of the described features. It may be possible that the clump feature in the north signifies the position of an accreting proto-planet with its own circumplanetary disk. If this is the case, the arc structure might be a spiral driven by the embedded planet in the outer disk (see e.g. Muto et al. 2012; Dong et al. 2016) and the over-brightness in the ALMA data may signify a density effect caused by a vortex also driven by the same planet. The correspondence between spirals in scattered light and asymmetries in dust continuum appears to be common among well studied disks (Garufi et al. 2018; van der Marel et al. 2021). Such a scenario may be confirmed with deeper SPHERE observations in better weather conditions, or with high spectral resolution ALMA gas line observations which may trace the local deviation from Keplerian rotation induced by an embedded planet (Pinte et al. 2018, 2020; Teague et al. 2018).

As we discuss in section **??** and show in figure 3, SY Cha is one of the group of disks for which we measure the highest aspect ratios. This typically should correspond to a bright signal in scattered light, as the disk surface intercepts more stellar light. However, as we show in figure 4 it is among the faintest detected disks in our sample. This apparent disagreement may be reconciled by the presence of the inner disk seen in the ALMA band 6 data in figure 14. In the same figure it is also visible that we receive the strongest scattered light signal close to the coronagraphic mask in the SPHERE scattered light observation. This signal may well originate from the inner disk. That the signal is more extended in scattered light than in ALMA mm continuum may be explained by radial drift of the larger dust particles (Weidenschilling 1977; Villenave et al. 2019). If the bright signal around the coronagraph indeed originates from the inner disk, then this indicates, that unlike the outer disk ring, it intercepts a lot of stellar light. The peak is particular strong toward the West, which we tentatively identified as the forward scattering side of the disk. If the inner disk is strongly flared (as we may expect from the measured aspect ratio of the outer disk ring) and is seen under slightly larger inclination than the outer disk, then this may explain the weak scattered light signal from the outer disk. A small relative misalignment between inner and outer disk would lead to a broad shadow cast on the outer disk ring (see e.g. Muro-Arena et al. 2020a for a detailed model of such an effect). If the inner disk has the same position angle of its major axis as the outer disk and is simply seen under a slightly larger inclination, then this broad shadow would fall on the forward scattering side of the outer disk, possibly up to the disk ansae, i.e. the regions in which we would typically expect the strongest scattered light signal. An inner disk seen under a high inclination may also explain the deviation of the angle of polarization from the interstellar dust induced polarization direction of the majority of Cha I sources and background stars seen through the Cha I cloud complex that we discuss in secion 4.1. Such a disk misalignment might fit well with the speculative presence of a massive planet at the disk clump location, if the orbit of such a planet was slightly misaligned with respect to the outer disk and thus is able to exert a torque on the disk warping or tilting the inner disk (Xiang-Gruess & Papaloizou 2013). Alternatively, the inner disk could simply be strongly puffed up due to stellar radiation, which may lead to full azimuthal shadowing of the outer disk, without the need to invoke a misalignment. However, it would then still be somewhat puzzling why the outer disk shows a high aspect ratio if it is mostly shielded from stellar radiation. High resolution ALMA gas line observations in the future may enable us to detect a possible warp or tilt between inner and outer disk. Alternatively near-infrared interferometric observation might be able to measure the inclination of the inner disk (Bohn et al. 2022).

5.7. SZ Cha

SZ Cha possess the most extended disk of our target sample (0.86 arcsec, i.e. 163 au). The disk shows a multi-ringed substructure with up to three discernible rings with semi-major axes at 0.20″, 0.36″ and 0.62″. The near side of the disk is located in the West with the semi-major axis at a position angle of 160°. Along the major axis there is some considerable brightness asymmetry between the Northern and the Southern part of the disk with a possible spiral feature present in the South and partially overlapping with the second ring-like feature. This geometry is reminiscent of the disk around the isolated Herbig star HD 34282 (de Boer et al. 2021). The geometry of the system is discussed in detail in the upcoming publication by Hagelberg et al., in prep.

5.8. VZ Cha

We find a low signal-to-noise detection of scattered light around VZ Cha. In figure B.1 it is visible that the Stokes Q and U images indeed show a butterfly pattern, with the majority of the signal located in the North-East lobe of the Stokes U image. Signal is detected out to a separation of 0.32″ (61 au). Transformation to Q_ϕ shows a faint disk with a position angle of ∼60°. Ellipse fitting yields an inclination of ∼51°. However, due to the low signal-to-noise the fit is highly uncertain (see figure C.3h). We placed several ellipses by eye that encompassed the existing signal and find a conservative range of 10° for both parameters.

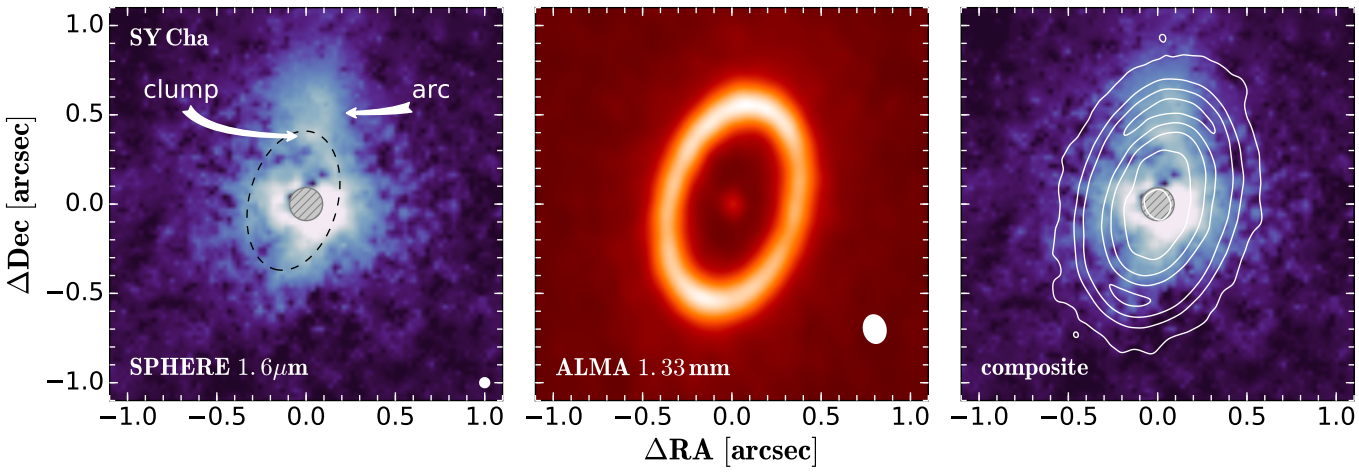

Fig. 14: *Left:* SPHERE/IRDIS polarized light H-band data of SY Cha. A variable Gaussian kernel was used to smooth the image. The data is shown on a logarithmic scale in order to highlight the disk morphology. The effective resolution element is shown on the lower right. We overlay an ellipse matching the ALMA inclination and position angle as black, dashed line and highlight two features near the northern ansae. *Middle:* ALMA dust continuum emission of SY Cha in Band 7 from Orihara et al. (submitted). The beam size is indicated by the white ellipse in the lower right corner. *Right:* ALMA data overlayed on top of the SPHERE data.

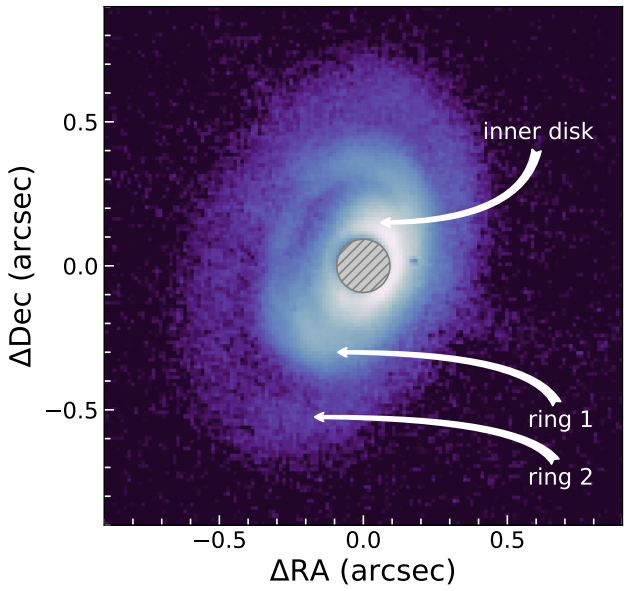

Fig. 15: Axial asymmetry of the disk surrounding HD 97048 relative to the minor axis from SPHERE K-band observations. We flipped the disk around its minor axis and then divided the original image by the flipped image. The ratio between the two is indicated by the color map. The white dashed line indicates the disk minor axis.

VZ Cha has a measured dust mass that is roughly a factor 2 higher than CV Cha which we detect at very high signal-to-noise (see table 1). CT Cha and SY Cha have comparable dust masses, and both were likewise detected with higher signal-to-noise than VZ Cha. Thus the low polarization signal is likely not connected to low dust surface density, but rather indicates that the disk around VZ Cha is significantly flatter than the other detected systems and thus intercepts less stellar light.

5.9. WW Cha

We resolve a compact disk and extended emission around WW Cha using the same data set that was already presented in Garufi et al. (2020). In particular the disk is dominated by a bright spiral arm extending from the South of the disk and winding clockwise. The width of the spiral arm decreases smoothly from the launching point to the tip of the detected emission in the West of the disk. It is thus not trivial to measure an opening angle.

Since the scattered light disk is extremely asymmetric it is not possible to extract reliable geometric properties from the data. However high resolution (89.6×60 mas beam size) ALMA band 7 data exists for the system, showing a symmetric disk in mm continuum emission, which were presented in Kanagawa et al. (2021). They used the ALMA data to extract inclination and position angle and found 64° for the former and 40.5° for the latter. The position angle is consistent with the scattered light data showing stronger elongation along North-East to South-West direction than in the perpendicular direction.

In addition to the Keplerian disk we find a complex structure of extended material some of which was already mentioned in Garufi et al. (2020). Most striking is the dark sickle or wedge shaped region extending form the North to the South clockwise. We have marked this region in figure 16.

Due to the asymmetry of the disk it is not trivial to determine whether the North-West or the South-East side of the disk is the near side. However the stellar position is clearly offset along the minor axis toward the North-West. Taking into account the height of the scattering surface this is a clear indication that the North-West is the near side of the disk and the South-East the far side (see e.g. de Boer et al. 2016). If this is true, then the dark wedge can be explained by a combination of the (not illuminated) disk mid-plane and an outer area of the disk which is either self shadowed or inherently faint. To clarify the geometry we show a sketch in figure 17.

The wedge if likely too wide in the North-West direction to be just the disk mid-plane (see e.g. Avenhaus et al. 2018; Garufi et al. 2020 for clear examples of the disk mid-plane). Further-

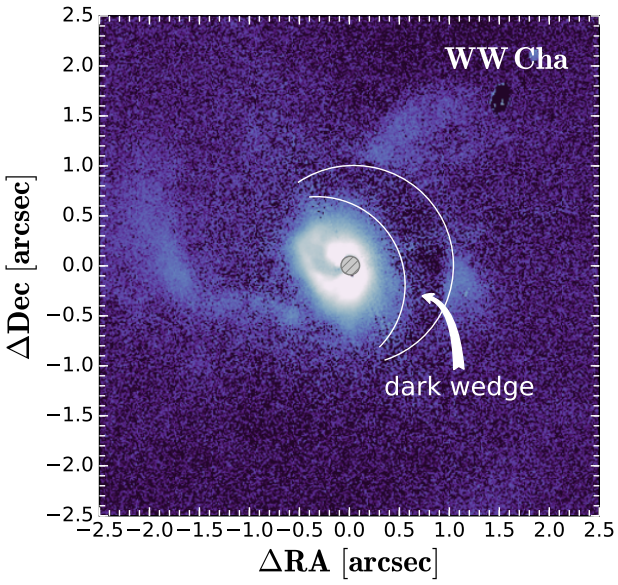

Fig. 16: Qϕ image of the WW Cha system from H-band observations. Extended dust structure is visible in polarized light beyond the circumstellar disk. A dark "wedge" sharply separates the disk from the extended material in the North-West direction.

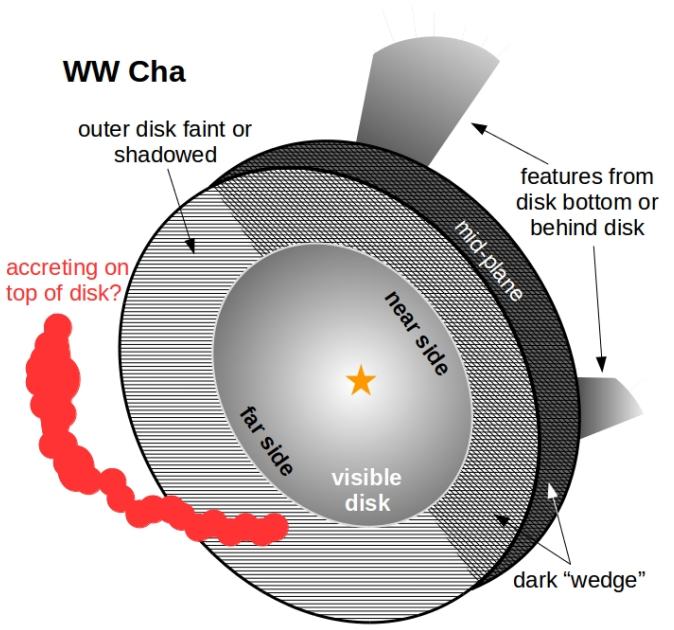

Fig. 17: Schematic of the WW Cha system geometry. The disk likely extends farther out in gas and small grains than it is detected in scattered light, either due to shadowing or due to the signal dropping below the noise threshold. The dark wedge in the data is caused by a combination of the unseen extended disk and the disk mid-plane.

more it does not appear that the wedge structure is converging to a point along the ansae as would be expected of the mid-plane and as shown in figure 17, although we caution that there is little signal in the ansae to fully trace the wedge. Yet the sharp transition between the dark wedge and the outer structures to the North-West and West suggest a geometric origin. If we assume that the top-side of the disk around WW Cha extends further than seen in scattered light, then a combination of this unseen outer part of the disk and the disk mid-plane can well explain the dark wedge region. This is displayed as the cross-hatched region in figure 17. If this picture is correct then the nebulous structures visible to the North-West and West beyond the dark wedge are either connected to the bottom side of the disk (the side facing away from the observer) or are part of the embedding cloud located behind the disk. Given that the structures are illuminated by WW Cha while other parts of the embedding cloud are not, it would follow that they can in any case not be arbitrarily far away from WW Cha.

The filamentary hook-shaped structure to the East of WW Cha was already noted by Garufi et al. (2020). If the interpretation of the dark wedge that we present is correct then the filament must be placed above the disk (i.e. in between the disk and the observer), otherwise we would not be able to trace it as close the the visible disk of WW Cha without it being obscured. In that case the filament might trace material infalling onto the disk as was recently shown for SU Aur (Ginski et al. 2021). Based on the Herschel far-infrared data shown in figure 1, WW Cha is located in one of the densest parts of the Cha I cloud, making an infall scenario likely. Deep ALMA gas emission line observations are needed to confirm the kinematics of the filament and other visible structures.

5.10. Non-detections

Of the 20 systems our sample seven yielded non-detections in polarized scattered light, i.e. either their disks are too small to be resolved with current instrumentation (radius < 92.5 mas, i.e. ~18 au at the average distance or Cha I), or too faint. Of these seven systems four are close visual binaries, i.e. DI Cha, PDS 51, WX Cha and WY Cha, with angular separations between xx mas and xx mas. For these systems it is plausible that the close stellar companions truncate the outer disk, and thus they are almost certainly in the first category of non-detections (small disks). Of the remaining three systems SZ 41 is a wide visual binary with an angular separation of ~2 arcsec (~380 au). It also has an exceptionally low dust mass with an upper limit of less than 1 $M_\oplus$, thus the disk in this system is likely small, but even if it where extended it would be faint with barely any dust entrained (assuming that the small *mu*m dust population roughly correlates with the mm-population detected at mm wavelength).

Finally CHX 18N and RXJ1106.3-7721 are single stars[6]. CHX 18N has a dust mass of 13 $M_\oplus$, which is at the lower end for our sample. However, the even lower mass disk around SZ 45 (10 $M_\oplus$) yielded a scattered light detection. The SED of CHX 18N does not show a significant dip close to 10*mu*m, indicating that this is still a full disk without a large cavity. In comparison SZ 45, shows a significant dip in the SED. Thus while we can not rule out that the disk around CHX 18N is simply compact it is possible that it is probable that it rather belongs to the 2nd category of non detections, i.e. faint (self shadowed) disks.

For RXJ1106.3-7721 we do not have a measured dust mass, however, the system shows no significant mid or far infrared excess emission, indicating that indeed no extended disk is present.

In summary of our non-detections we find that 5 are in all likelihood compact. One is faint and possibly self-shadowed and

[6] No companions are reported in the literature and we do not detect any close stellar companion candidates within our SPHERE imaging data

one might be either compact or faint. The majority of compact disks (4/5) is found (somewhat unsurprisingly) in close visual binary systems.

6. Summary and discussion

We observed a sample of 20 systems in the nearby Chamaeleon I star forming region with VLT/SPHERE in polarized scattered light. Our observations revealed resolved circumstellar structure around 13 of these systems. Of these the HD 97048, SZ Cha and the WW Cha system showed clear morphological sub-structures, while we tentatively find shadow features in CV Cha and a possible dust clump and arc in the SY Cha system. The CR Cha, CS Cha, CT Cha, SZ 45, TW Cha and VZ Cha systems all show relatively small disks that appear largely smooth at our spatial resolution and sensitivity, but that vary by a factor of ∼4 in polarized brightness contrast relative to the central star. We find a tentative trend between the "transitional" nature of the system SED (the presence of a dip at $\sim 10 \mu m$) and the brightness in scattered light, with the two classical transitional disks (based on their SED) around CS Cha and HD 97048 being the brightest disks in our sample. We find a possible correlation of this trend with the dust mass in the system. However, the dust masses of CR Cha and VZ Cha are similar or even slightly larger than for the bright disk around CS Cha. Yet both of these former systems are significantly fainter in scattered light, with VZ Cha being the faintest detected disk in our sample. This suggest that the brightness in scattered light is at least in some cases dominated by geometric shadowing effects by inner-system material rather than overall depletion. This conclusion is in line with the very recent findings of Garufi et al. (2022), who studied a sample of 15 disk that are faint in scattered light and found an anti-correlation between the amount of near-infrared excess and the brightness in near-infraed scattered light.

Since the scattered light brightness of the disks appears to be linked to the opening of a cavity in the inner disk region it is interesting to study its age dependence. From our sample we do not recover a clear trend between system age and scattered light brightness. However, 12 of the 14 systems that are younger than 2 Myr are all faint in scattered light. The exceptions are the WW Cha system, which appears to be still interacting with surrounding cloud material, and the extremely flaring SZ Cha system. The two bright transition disks within our sample, CS Cha and HD 97048, are among the oldest systems within our sample. These general findings are consistent with the findings of Garufi et al. (2018), who looked at a larger sample of scattered light disks inhomogeneously drawn from multiple star forming regions and isolated stars. However, their sample was by construction biased toward known bright transition disks. A larger unbiased sample size is needed in order to draw clear conclusion on the connection between disk brightness and stellar age. A possible correlation of scattered light brightness and system age paints an interesting picture. Young disks at the start of planet formation may still be faint in scattered light, because the forming proto-planets have not yet opened a gap or cavity in the inner disk. When planetary cores have formed, the disk becomes increasingly bright in scattered light due to the lack of shadowing material in the inner disk regions. The increased illumination of the outer disk may in turn lead also to an increase in temperature and disk flaring. A similar scenario was speculated upon in the context of mid-infrared interferometric observations by Menu et al. (2015). The oldest system in our study, the CS Cha system, might be an extreme case of such an evolution, due to the circumbinary nature of the disk. We note that indeed known circumbinary disks in the literature tend to be bright in scattered light, for example the disks around HD 34700 (Monnier et al. 2019), GG Tau (Krist et al. 2002; Itoh et al. 2014; Keppler et al. 2020) or HD 142527 (Fukagawa et al. 2006; Avenhaus et al. 2014; Hunziker et al. 2021).

Given the orbit constraints we can put on the inner stellar companion in the CS Cha system, it appears possible that it is responsible for opening the cavity within the disk, seen in ALMA mm continuum emission and also evident from the system SED, although an additional planet might be needed to explain the disk asymmetry seen in ALMA dust continuum (Kurtovic et al., submitted). Our polarized scattered light color analysis suggests that the disk around CS Cha consist of small compact aggregates which are relatively settled. This is well consistent with numerical simulations that suggest that the binary companion will excite eccentric dust particle orbits, which lead to orbit crossing and collisions with speeds above fragmentation velocity (Meschiari 2012; Paardekooper et al. 2012; Pierens et al. 2021). In a recent study, using three dimensional hydrodynamic simulations Pierens et al. (2021) also found that the dust scale height near the tidally truncated cavity edge is low, especially for high solid-to-gas ratios. That the dust grains in the disk are already in an advanced stage of settling fits well with the very small aspect ratio of ∼0.03 that we find at a radius of 85 au (although we note that this value comes with a large uncertainty as discussed in section 4.2). This is in turn also well consistent with the picture of a rather old disk (3-5.3 Myr). The fact that we observe grain segregation in the CS Cha disk, with a narrow ring and large cavity in mm-emission, and no resolved cavity in scattered light, might be explained by the circumbinary nature of this system (see e.g. de Juan Ovelar et al. 2013). We note that the disk-mass normalized accretion rate of CS Cha is among the lowest in the sample, which may indicate that the disk is somewhat depleted in gas compared to the younger systems.

Considering that the age of the WW Cha system is comparable to the CR Cha, CV Cha and SY Cha systems, which show much fainter scattered light disks, it appears to be an outlier in the age - disk brightness correlation. However, this system seems to still interact with surrounding cloud material, seen in scattered light. This was already pointed out by Garufi et al. (2020), who note that the system is located in a known network of clumpy filaments (Haikala et al. 2005). The morphology, with possible streamers connected to the disk, as seen in scattered light, is somewhat reminiscent of the case of SU Aur, where late infall of material was recently shown by Ginski et al. (2021). If this is the case the disk in WW Cha might well be "second generation" rather than "primordial" and thus may not follow the general evolutionary trend of the other Cha I systems. Deep, high spatial resolution molecular line observations with ALMA could shed light on the nature of the interaction of WW Cha with the surrounding cloud.

Our high spatial resolution, near-infrared study of Cha I systems has shown some interesting trends that connect the scattered light appearance of the circumstellar disks with the disk evolution. It will be most interesting to compare these findings with similar studies of other nearby star forming regions. We are currently attempting this in the framework of the Disk Evolution Study Through Imaging of Nearby Young Stars program (DESTINYS, Ginski et al. 2020, 2021), carried out with VLT/SPHERE, VLT/X-Shooter and ALMA. Companion papers to this study, focusing on the Taurus star forming region as well as the Orion star forming region are currently under review (Garufi et al., submitted; Valegard et al., submitted). Furthermore, it will be critical in the future to enable similar ob-

servations of optically fainter low-mass stars, i.e. the bulk of the stellar content of Cha I and other nearby star forming regions. This may be enabled by the SPHERE+ initiative (Boccaletti et al. 2020), which aimes to upgrade the SPHERE AO system to observe fainter and redder objects.

Acknowledgements. Based on observations made with ESO Telescopes at the La Silla Paranal Observatory under programme ID XX.XXXX This work has made use of data from the European Space Agency (ESA) mission *Gaia* (https://www.cosmos.esa.int/gaia), processed by the *Gaia* Data Processing and Analysis Consortium (DPAC, https://www.cosmos.esa.int/web/gaia/dpac/consortium). Funding for the DPAC has been provided by national institutions, in particular the institutions participating in the *Gaia* Multilateral Agreement. SPHERE was designed and built by a consortium made of IPAG (Grenoble, France), MPIA (Heidelberg, Germany), LAM (Marseille, France), LESIA (Paris, France), Laboratoire Lagrange (Nice, France), INAF–Osservatorio di Padova (Italy), Observatoire de Genève (Switzerland), ETH Zurich (Switzerland), NOVA (Netherlands), ONERA (France) and ASTRON (Netherlands) in collaboration with ESO. SPHERE was funded by ESO, with additional contributions from CNRS (France), MPIA (Germany), INAF (Italy), FINES (Switzerland) and NOVA (Netherlands). Additional funding from EC's 6th and 7th Framework Programmes as part of OPTICON was received (grant number RII3-Ct-2004-001566 for FP6 (2004–2008); 226604 for FP7 (2009–2012); 312430 for FP7 (2013–2016)). N.K. and P.P. acknowledges support provided by the Alexander von Humboldt Foundation in the framework of the Sofja Kovalevskaja Award endowed by the Federal Ministry of Education and Research. This paper makes use of the following ALMA data: ADS/JAO.ALMA2018.1.00689.S. ALMA is a partnership of ESO (representing its member states), NSF (USA) and NINS (Japan), together with NRC (Canada), MOST and ASIAA (Taiwan), and KASI (Republic of Korea), in cooperation with the Republic of Chile. The Joint ALMA Observatory is operated by ESO, AUI/NRAO and NAOJ.

References

Andrews, S. M., Wilner, D. J., Espaillat, C., et al. 2011, ApJ, 732, 42
Ansdell, M., Williams, J. P., Manara, C. F., et al. 2017, AJ, 153, 240
Ansdell, M., Williams, J. P., van der Marel, N., et al. 2016, ApJ, 828, 46
Artymowicz, P. & Lubow, S. H. 1994, ApJ, 421, 651
Avenhaus, H., Quanz, S. P., Garufi, A., et al. 2018, ApJ, 863, 44
Avenhaus, H., Quanz, S. P., Schmid, H. M., et al. 2014, ApJ, 781, 87
Ballering, N. P. & Eisner, J. A. 2019, AJ, 157, 144
Baraffe, I., Homeier, D., Allard, F., & Chabrier, G. 2015a, A&A, 577, A42
Baraffe, I., Homeier, D., Allard, F., & Chabrier, G. 2015b, A&A, 577, A42
Beckwith, S. V. W. & Sargent, A. I. 1991, ApJ, 381, 250
Benisty, M., Stolker, T., Pohl, A., et al. 2017, A&A, 597, A42
Beuzit, J. L., Vigan, A., Mouillet, D., et al. 2019, A&A, 631, A155
Blunt, S., Wang, J. J., Angelo, I., et al. 2020, AJ, 159, 89
Boccaletti, A., Chauvin, G., Mouillet, D., et al. 2020, arXiv e-prints, arXiv:2003.05714
Bohn, A. J., Benisty, M., Perraut, K., et al. 2022, A&A, 658, A183
Bohn, A. J., Southworth, J., Ginski, C., et al. 2020, A&A, 635, A73
Bressan, A., Marigo, P., Girardi, L., et al. 2012, MNRAS, 427, 127
Canovas, H., Rodenhuis, M., Jeffers, S. V., Min, M., & Keller, C. U. 2011, A&A, 531, A102
Carbillet, M., Bendjoya, P., Abe, L., et al. 2011, Experimental Astronomy, 30, 39
Choi, J., Dotter, A., Conroy, C., et al. 2016, ApJ, 823, 102
Cieza, L. A., Ruíz-Rodríguez, D., Hales, A., et al. 2019, MNRAS, 482, 698
Covino, E., Palazzi, E., Penprase, B. E., Schwarz, H. E., & Terranegra, L. 1997, A&AS, 122, 95
Dawson, R. I., Murray-Clay, R. A., & Fabrycky, D. C. 2011, ApJ, 743, L17
de Boer, J., Ginski, C., Chauvin, G., et al. 2021, A&A, 649, A25
de Boer, J., Langlois, M., van Holstein, R. G., et al. 2020, A&A, 633, A63
de Boer, J., Salter, G., Benisty, M., et al. 2016, A&A, 595, A114
de Juan Ovelar, M., Min, M., Dominik, C., et al. 2013, A&A, 560, A111
Doering, R. L., Meixner, M., Holfeltz, S. T., et al. 2007, AJ, 133, 2122
Dohlen, K., Langlois, M., Saisse, M., et al. 2008, in Proc. SPIE, Vol. 7014, Ground-based and Airborne Instrumentation for Astronomy II, 70143L
Dominik, C., Min, M., & Tazaki, R. 2021, OpTool: Command-line driven tool for creating complex dust opacities
Dong, R., Fung, J., & Chiang, E. 2016, ApJ, 826, 75
Dullemond, C. P. & Dominik, C. 2004, A&A, 417, 159
Dullemond, C. P., Juhasz, A., Pohl, A., et al. 2012, RADMC-3D: A multi-purpose radiative transfer tool
Engler, N., Schmid, H. M., Thalmann, C., et al. 2017, A&A, 607, A90
Foreman-Mackey, D., Hogg, D. W., Lang, D., & Goodman, J. 2013, PASP, 125, 306
Francis, L. & van der Marel, N. 2020, ApJ, 892, 111
Fukagawa, M., Tamura, M., Itoh, Y., et al. 2006, ApJ, 636, L153
Gaia Collaboration, Brown, A. G. A., Vallenari, A., et al. 2018, A&A, 616, A1
Gaia Collaboration, Vallenari, A., Brown, A. G. A., et al. 2022, arXiv e-prints, arXiv:2208.00211
Garufi, A., Avenhaus, H., Pérez, S., et al. 2020, A&A, 633, A82
Garufi, A., Benisty, M., Pinilla, P., et al. 2018, A&A, 620, A94
Garufi, A., Dominik, C., Ginski, C., et al. 2022, A&A, 658, A137
Garufi, A., Meeus, G., Benisty, M., et al. 2017, A&A, 603, A21
Garufi, A., Quanz, S. P., Schmid, H. M., et al. 2014, A&A, 568, A40
Garufi, A., Quanz, S. P., Schmid, H. M., et al. 2016, A&A, 588, A8
Ginski, C., Benisty, M., van Holstein, R. G., et al. 2018, A&A, 616, A79
Ginski, C., Facchini, S., Huang, J., et al. 2021, ApJ, 908, L25
Ginski, C., Ménard, F., Rab, C., et al. 2020, A&A, 642, A119
Ginski, C., Stolker, T., Pinilla, P., et al. 2016, A&A, 595, A112
Grady, C. A., Polomski, E. F., Henning, T., et al. 2001, AJ, 122, 3396
Guenther, E. W., Esposito, M., Mundt, R., et al. 2007, A&A, 467, 1147
Haikala, L. K., Harju, J., Mattila, K., & Toriseva, M. 2005, A&A, 431, 149
Halíf, R. & Flusser, J. 1998
Hartmann, L., Calvet, N., Gullbring, E., & D'Alessio, P. 1998, ApJ, 495, 385
Hauschildt, P. H., Allard, F., & Baron, E. 1999, ApJ, 512, 377
Hunziker, S., Schmid, H. M., Ma, J., et al. 2021, A&A, 648, A110
Itoh, Y., Oasa, Y., Kudo, T., et al. 2014, Research in Astronomy and Astrophysics, 14, 1438
Jones, M. I., Milli, J., Blanchard, I., et al. 2022, arXiv e-prints, arXiv:2204.11746
Kanagawa, K. D., Hashimoto, J., Muto, T., et al. 2021, ApJ, 909, 212
Kendall, M. G. 1938, Biometrika, 30, 81
Keppler, M., Penzlin, A., Benisty, M., et al. 2020, A&A, 639, A62
Kim, S., Takahashi, S., Nomura, H., et al. 2020, ApJ, 888, 72
Kiraga, M. 2012, Acta Astron., 62, 67
Krist, J. E., Stapelfeldt, K. R., & Watson, A. M. 2002, ApJ, 570, 785
Kurtovic, N. T., Pinilla, P., Penzlin, A. B. T., et al. 2022, A&A, 664, A151
Lagage, P.-O., Doucet, C., Pantin, E., et al. 2006, Science, 314, 621
Langlois, M., Dohlen, K., Vigan, A., et al. 2014, in Proc. SPIE, Vol. 9147, Ground-based and Airborne Instrumentation for Astronomy V, 91471R
Long, F., Herczeg, G. J., Harsono, D., et al. 2019, ApJ, 882, 49
Manara, C. F., Fedele, D., Herczeg, G. J., & Teixeira, P. S. 2016, A&A, 585, A136
Manara, C. F., Mordasini, C., Testi, L., et al. 2019, A&A, 631, L2
Marino, S., Perez, S., & Casassus, S. 2015, ApJ, 798, L44
Martinez, P., Dorrer, C., Aller Carpentier, E., et al. 2009, A&A, 495, 363
Meeus, G., Waters, L. B. F. M., Bouwman, J., et al. 2001, A&A, 365, 476
Menu, J., van Boekel, R., Henning, T., et al. 2015, A&A, 581, A107
Meschiari, S. 2012, ApJ, 761, L7
Monnier, J. D., Harries, T. J., Bae, J., et al. 2019, ApJ, 872, 122
Muro-Arena, G. A., Benisty, M., Ginski, C., et al. 2020a, A&A, 635, A121
Muro-Arena, G. A., Ginski, C., Dominik, C., et al. 2020b, A&A, 636, L4
Muto, T., Grady, C. A., Hashimoto, J., et al. 2012, ApJ, 748, L22
Orihara, R., Momose, M., Muto, T., et al. 2023, PASJ, 75, 424
Paardekooper, S.-J., Leinhardt, Z. M., Thébault, P., & Baruteau, C. 2012, ApJ, 754, L16
Pascucci, I., Testi, L., Herczeg, G. J., et al. 2016, ApJ, 831, 125
Pierens, A., Nelson, R. P., & McNally, C. P. 2021, MNRAS
Pineda, J. E., Quanz, S. P., Meru, F., et al. 2014, ApJ, 788, L34
Pinte, C., Price, D. J., Ménard, F., et al. 2020, ApJ, 890, L9
Pinte, C., Price, D. J., Ménard, F., et al. 2018, ApJ, 860, L13
Pinte, C., van der Plas, G., Ménard, F., et al. 2019, Nature Astronomy, 3, 1109
Ribas, Á., Espaillat, C. C., Macías, E., et al. 2017, ApJ, 849, 63
Ribas, Á., Espaillat, C. C., Macías, E., & Sarro, L. M. 2020, A&A, 642, A171
Rich, E. A., Monnier, J. D., Aarnio, A., et al. 2022, AJ, 164, 109
Rich, E. A., Teague, R., Monnier, J. D., et al. 2021, ApJ, 913, 138
Schmid, H. M., Bazzon, A., Roelfsema, R., et al. 2018, A&A, 619, A9
Schmid, H. M., Joos, F., & Tschan, D. 2006, A&A, 452, 657
Serkowski, K., Mathewson, D. S., & Ford, V. L. 1975, ApJ, 196, 261
Siess, L., Dufour, E., & Forestini, M. 2000, A&A, 358, 593
Smart, R. L. & Nicastro, L. 2014, A&A, 570, A87
Stolker, T., Dominik, C., Avenhaus, H., et al. 2016, A&A, 595, A113
Tazaki, R., Tanaka, H., Muto, T., Kataoka, A., & Okuzumi, S. 2019, MNRAS, 485, 4951
Teague, R., Bae, J., Bergin, E. A., Birnstiel, T., & Foreman-Mackey, D. 2018, ApJ, 860, L12
van der Marel, N., Birnstiel, T., Garufi, A., et al. 2021, AJ, 161, 33
van der Marel, N., Cazzoletti, P., Pinilla, P., & Garufi, A. 2016, ApJ, 832, 178
van der Plas, G., Wright, C. M., Ménard, F., et al. 2017a, A&A, 597, A32
van der Plas, G., Wright, C. M., Ménard, F., et al. 2017b, A&A, 597, A32
van Holstein, R. G., Girard, J. H., de Boer, J., et al. 2020, A&A, 633, A64
van Holstein, R. G., Stolker, T., Jensen-Clem, R., et al. 2021, A&A, 647, A21
Villenave, M., Benisty, M., Dent, W. R. F., et al. 2019, A&A, 624, A7
Voirin, J., Manara, C. F., & Prusti, T. 2018, A&A, 610, A64
Walsh, C., Juhász, A., Meeus, G., et al. 2016, ApJ, 831, 200
Walsh, C., Juhász, A., Pinilla, P., et al. 2014, ApJ, 791, L6
Weidenschilling, S. J. 1977, Ap&SS, 51, 153
Xiang-Gruess, M. & Papaloizou, J. C. B. 2013, MNRAS, 431, 1320
Zhang, Y., Ginski, C., Huang, J., et al. 2023, A&A, 672, A145

Appendix A: Observing condition and instrument setup

The detailed dates and weather conditions of our observations as well as the instrument setup are listed in Table A.1.

Table A.1: Observing dates, instrument setup and weather conditions for all systems in our study.

Target	Date	Filter	Coronagraph	DIT [s]	# frames	Seeing [arcsec]	τ_0 [ms]
CHX 18 N							
CHX 22							
CR Cha	15-01-2019	BB_H	N_ALC_YJH_S	32	16	0.65	5.4
	15-01-2019	BB_H	none	0.83	480	0.65	5.4
CS Cha	17-02-2017	BB_J	N_ALC_YJH_S	96	40		
	17-06-2017	BB_H	N_ALC_YJH_S	64	28		
	23-12-2018	I_PRIM/R_PRIM	V_CLC_MT_WF	10	120	0.65	5.9
	20-01-2019	I_PRIM/R_PRIM	V_CLC_MT_WF	58	32	0.55	10.5
	24-03-2019	BB_K	N_ALC_YJH_S	64	28	0.70	8.8
CT Cha	25-02-2018	BB_H	N_ALC_YJH_S	64			
CV Cha	26-03-2016	BB_J	N_ALC_YJ_S	64	48		
	26-03-2016	BB_J + ND_1.0	none	2	240		1.3
DI Cha							
HD97048							
HP Cha							
PDS 51							
RX J1106.3-7721							
SY Cha	16-05-2017	BB_H	N_ALC_YJH_S	64	32	0.75	-
Sz 41							
Sz 45							
SZ Cha	21-03-2017	BB_H	N_ALC_YJH_S	96	20	0.70	-
TW Cha							
VZ Cha	28-02-2018	BB_H	N_ALC_YJH_S	64	12		
WW Cha	12-03-2017	BB_H	N_ALC_YJH_S	32	48	0.50	-
WX Cha	01-04-2019	BB H	none	0.83	480	0.85	3.0
WY Cha	18-02-2019	BB H	none	0.83	480	0.65	15

Appendix B: Detailed Stokes images

In this section we show the Stokes Q and U images that are directly measured in our observations. For all coronagraphic observations we summarize them in figure B.1 and for non-coronagraphic observations in figure B.2. Due to the azimuthal orientation of the angle of polarization of single scattered light, we expect a typical "butterfly" pattern in the Q and U images in which we detect resolved disk signal. This is indeed the case for all our coronagraphic observations, as well as the non-coronagraphic observations of CR Cha and CV Cha. In addition to Stokes Q and U we also show the derived Q_ϕ and U_ϕ images. As predicted from single scattering models the U_ϕ images contain little signal. For the coronagraphic observations we show the Q_ϕ images with different scaling to bridge the dynamic range between bright inner and fainter outer structures. In the 5th column of figure B.1 we compensate for the drop in stellar illumination by scaling the signal with the squared distance from the central star. We take into account the inclination of the disk to prevent the introduction of nonphysical asymmetries between major and minor disk axis. However, we caution that we did not take into account the disk scale height for the correction, as the surface height profile is uncertain for most objects. Alternatively in the 6th panel of figure B.1 we show the same images with a logarithmic scaling, which allows to display a larger dynamic range without a priory knowledge of the disk geometry. In figure B.2 we additionally show the total intensity images of the non-coronagraphic system. The binary stellar companions to WX Cha and WY Cha are clearly visible.

Appendix C: Geometric fitting approach and results

In this section we briefly demonstrate the validity of our fitting approach as described in section 4.2 and illustrate the extracted data points and best fitting ellipse solutions from the initial fitting step.

While it was demonstrated in the literature that equidistant rings can be used to constrain the disk geometry in scattered light images, this was not yet done for small, essentially feature-less (or in any case "ring-less") disks. For this purpose we created a grid of radiative transfer models with two different flaring exponents (1.09 and 1.3), simulating relatively flat and strongly flared disks. The disks are smooth and featureless. Within the grid we vary the inclination of the disk to demonstrate how the recovery of disk parameters is dependent on the viewing geometry. We show the model images in Figure C.1. Before testing our fitting procedure we convolved each model image with a Gaussian to simulate the resolution of VLT/SPHERE in the H-band. We then added noise to the images by co-adding the model image with a typical reduced image of a disk non-detection. The scaling of the disk forward scattering side and the background noise level was such that the resulting signal to noise ratios were comparable to those of the observed disks in our sample, in particular the case of CR Cha, which is faint but still well detected. We then ran the two-step fitting procedure, as described in section **??** on all model images. We show the extracted inclination, position angle and disk aspect ratio as a function of the model disk inclination in Figure C.2. Extracted inclination and position angle are from the first LSMC step. The extracted aspect ratio is measured with the second aperture photometry step, with inclination and position angle of the model fixed. We find that for inclinations larger than $\sim 10°$ the measured inclination and position angle are well consistent with the expected results. For small inclinations below $\sim 30°$ the uncertainty on the position angle in particular is large and appears somewhat inflated for values in between 10° and 30°. The measured aspect ratio shows little variation for the case of the strongly flaring disk (β=1.3) as a function of model inclination. We do however observe a small systematic offset of ~ 0.05, i.e. the retrieved aspect ratio is slightly too small. This is likely an effect of the polarized phase function, which leads to a weak signal on the far side of the disk, which can lead to systematically smaller offset values found by the aperture method (we note the same would be expected for the pure edge tracing method for the same reason). For the less flaring disks (β=1.09) we find small variability within the retrieved aspect ratios as a function of model inclination. This is to be expected as the offset values are smaller for flatter disks and thus inherently harder to measure. Within the uncertainties all values are however consistent with each other. We find the same systematic offset for this case as for the strong flaring case, i.e. aspect ratios are roughly too small by ~ 0.05.

In Figures C.3 and C.4 we show the extracted data points and best fitting LSMC ellipses for our data. We note that we intentionally display the data in a saturated color map to highlight the disk edge.

Appendix D: Spectral energy distributions for sample systems

In this appendix we show the spectral energy distributions for all sources included in our survey. The displayed data includes broad-band photometry (black data points), Spitzer/IRS spectra (red lines) and, if available, Herschel/SPIRE spectra (green lines). The data collection is taken from Ribas et al. (2017) (with references therein) for all sources but SY Cha, for which we did a similar data collection in this work.

Appendix E: CS Cha radiative transfer models

We show the simulated scattered light images produced from the radiative transfer models utilized in the CS Cha color analysis discussed in section 5.2.1.

Appendix F: CS Cha Aab orbit fit

We show the results of the orbit fits of the inner stellar binary in the CS Cha system, discussed in section 5.2.2. In figure F.1 we show a random selection of 10 possible orbits drawn from the posterior distribution of orbit elements. The top panels show the apparent orbits in R.A. - Dec space as well as separation - position angle space. The bottom panel shows the radial velocity of the primary star. In figure F.2 we show the resulting posterior distributions of the orbit fot for the semi-major axis, inclination and eccentricity. Displayed are the 95 % intervals for each parameter.

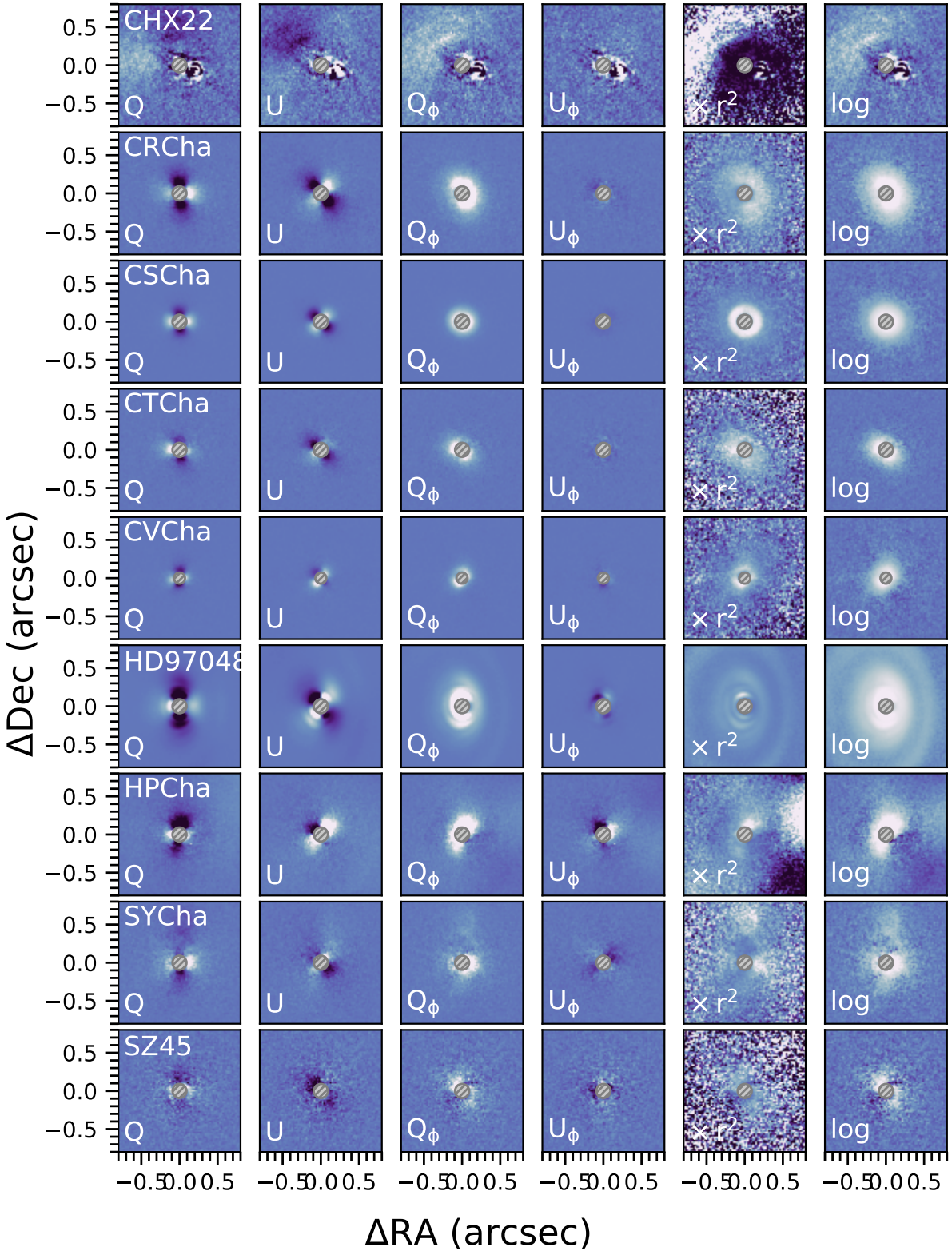

Fig. B.1: All coronagraphic images of our target sample. The color scale is linear in all images with the same cuts in each row but different cuts for different sources. The color scale is symmetric around 0. The grey hashed circles show the coronagraph size and position. We show the Stokes Q and U images in the first two columns and the derived Q_ϕ and U_ϕ images in column 3 and 4. In the fifth column we show the Q_ϕ image corrected for the separation dependent drop-off in illumination (taking into account the system inclination). In the last column we show the Q_ϕ image on a log scale, to highlight the fainter parts of the disks.

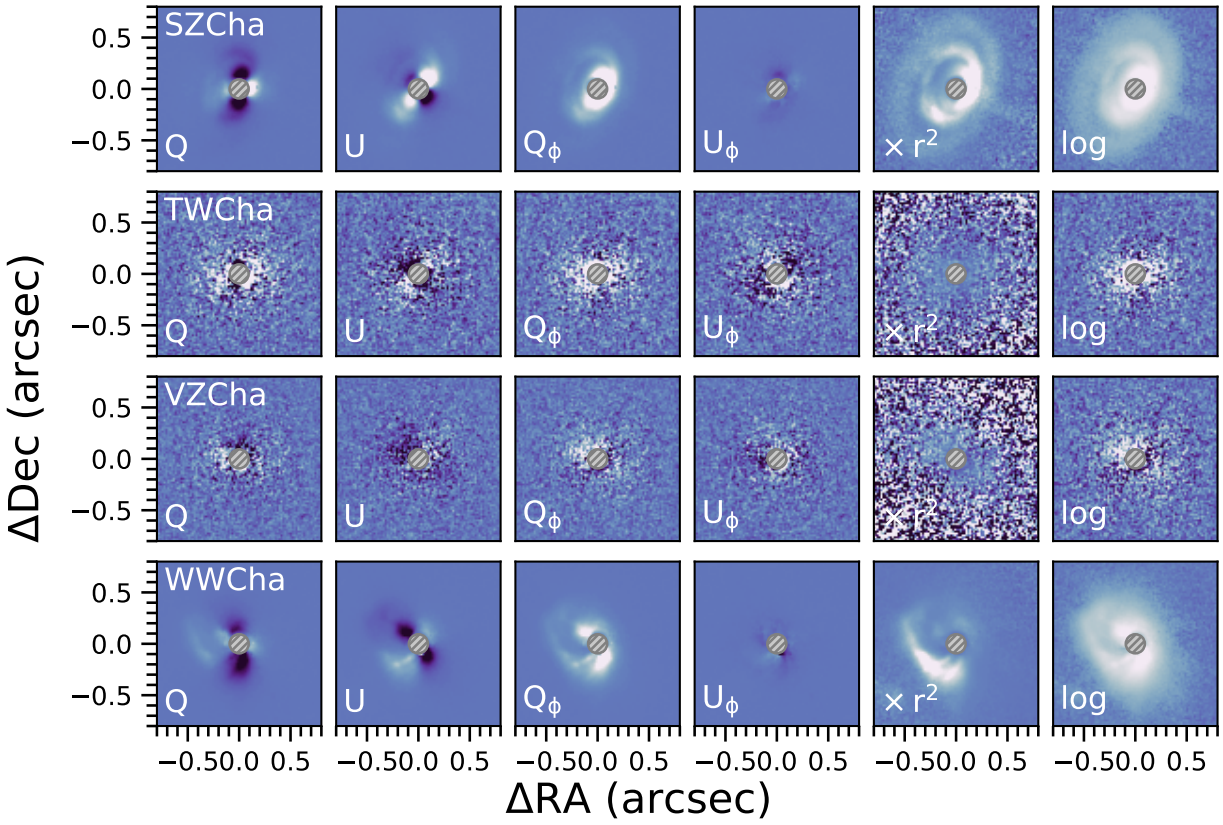

Fig. B.1: **(continued)** All coronagraphic images of our target sample. The color scale is linear in all images with the same cuts in each row but different cuts for different sources. The color scale is symmetric around 0. The grey hashed circles show the coronagraph size and position. We show the Stokes Q and U images in the first two columns and the derived Q_ϕ and U_ϕ images in column 3 and 4. In the fifth column we show the Q_ϕ image corrected for the separation dependent drop-off in illumination (taking into account the system inclination). In the last column we show the Q_ϕ image on a log scale, to highlight the fainter parts of the disks.

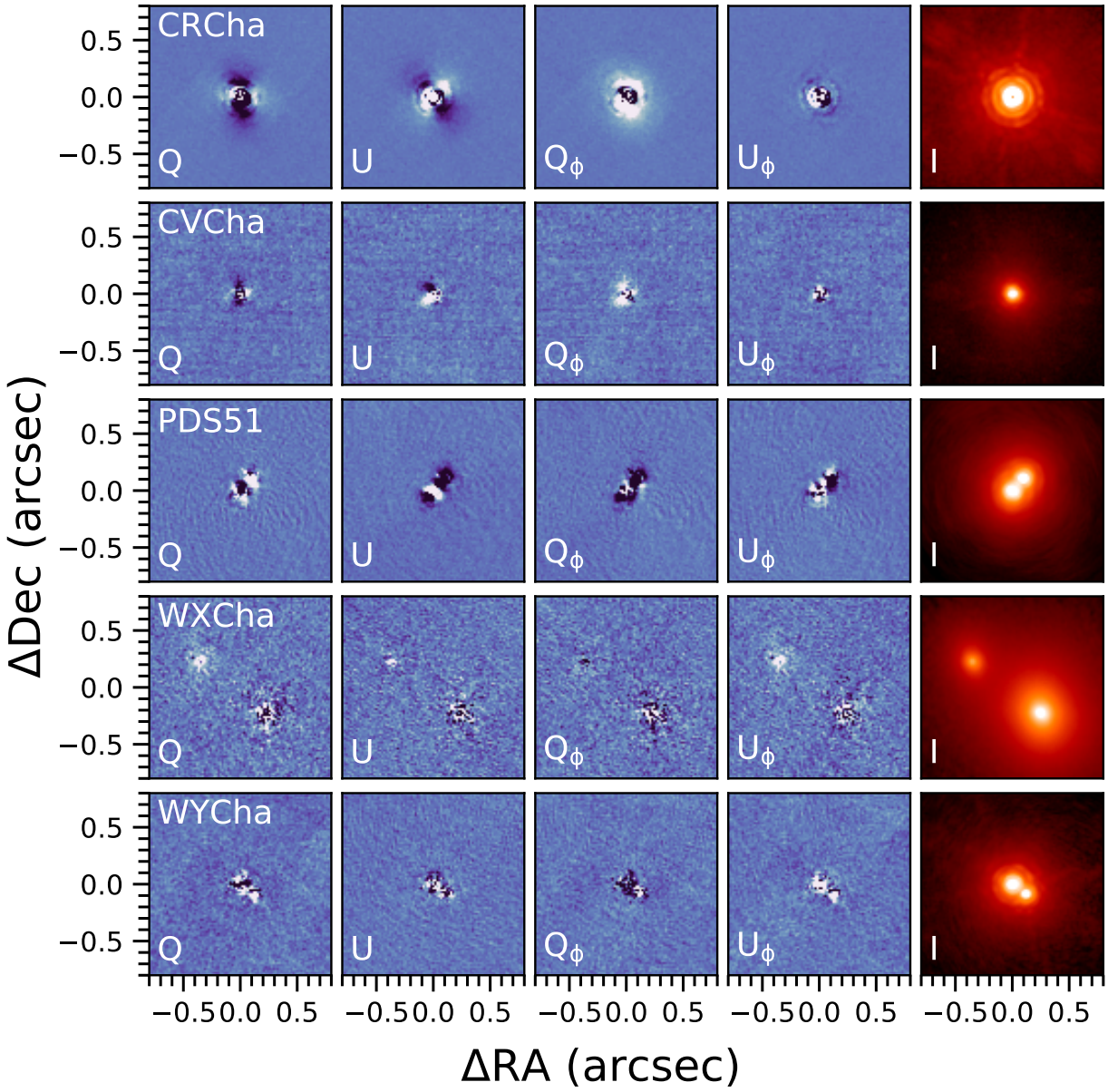

Fig. B.2: All non-coronagraphic images of our target sample. The color scale is linear in all images with the same cuts for all images. The color scale is symmetric around 0. The final column in each row in the red-orange hues shows the total intensity images in which the stellar light dominates. For WX Cha and WY Cha close stellar binary companions are visible in the data.

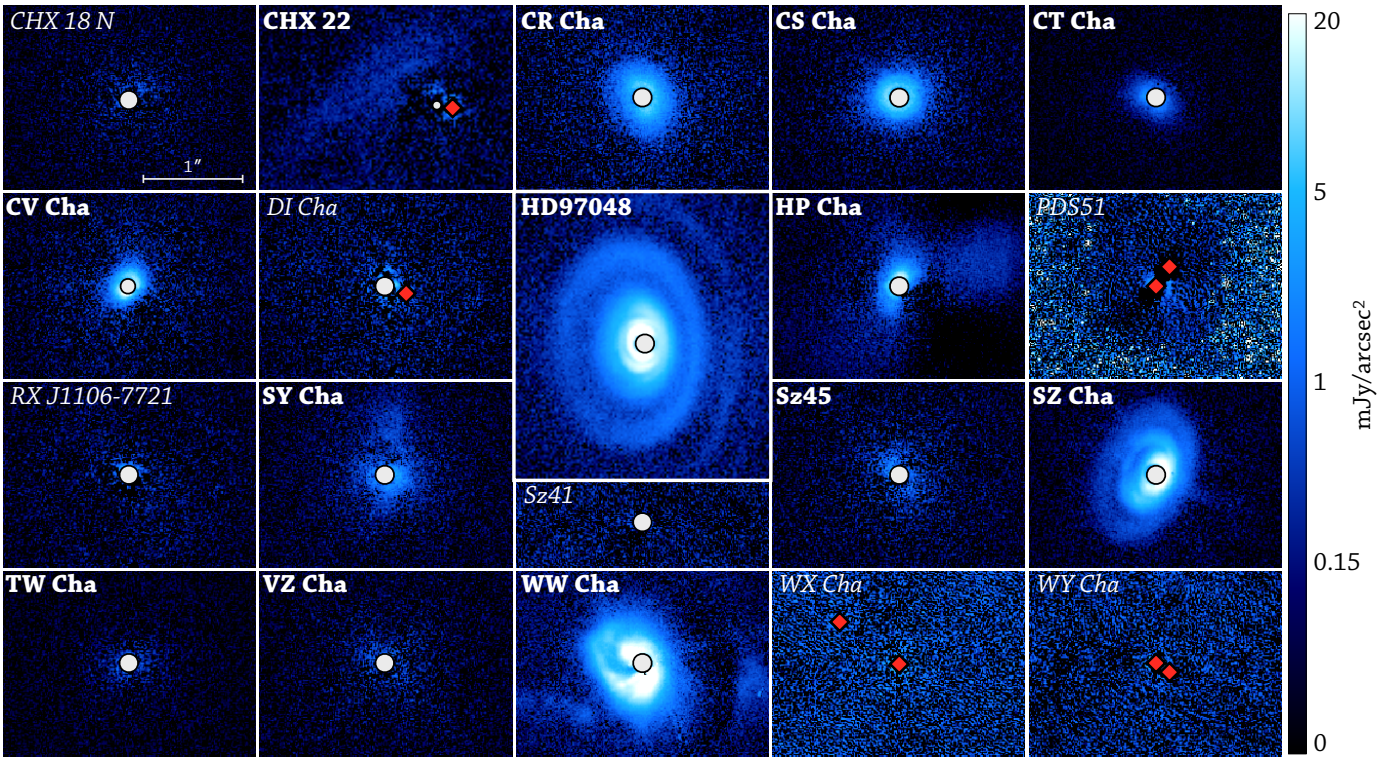

Fig. B.3: Imagery of the sample. The Q_ϕ image of all targets is shown at the same logarithmic, flux scale and physical scale (as indicated in the first panel). Detections are indicated by a name in bold, non-detections in italic. The grey circles mark the size of the coronagraphic mask while the red diamonds the position of any unmasked star (both primary in non-coronagraphic observations and companions).

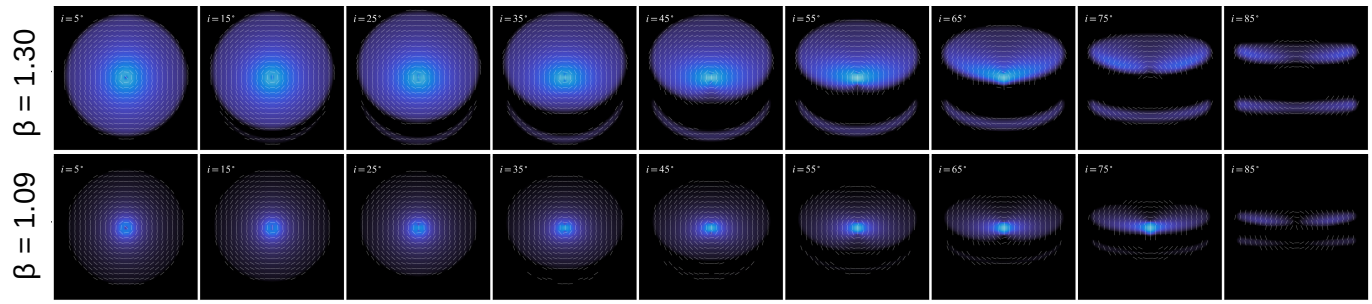

Fig. C.1: Radiative transfer polarized intensity model images with different flaring exponents β seen at different inclinations.

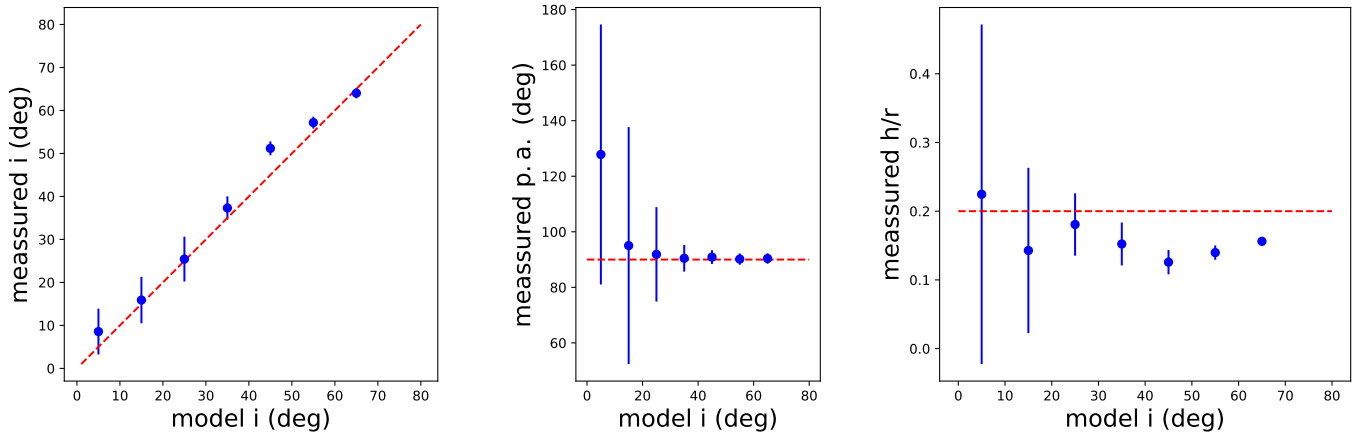

(a) Fits for $\beta = 1.09$

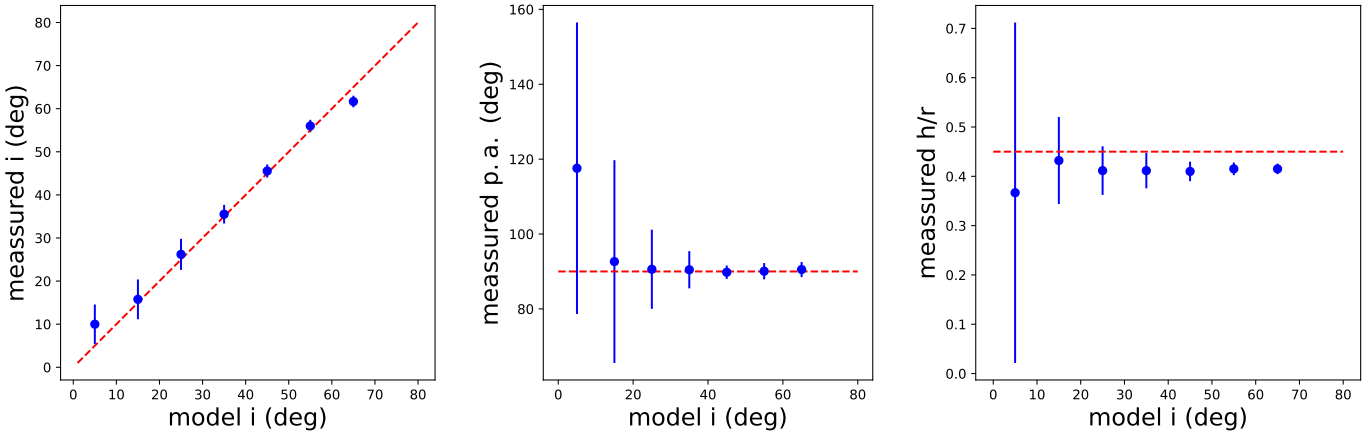

(b) Fits for $\beta = 1.30$

Fig. C.2: Ellipse fit to the outer disk edge for our radiative transfer model images. Fitting results are shown as function of model inclination. The expected results are indicated by the red-dashed lines.

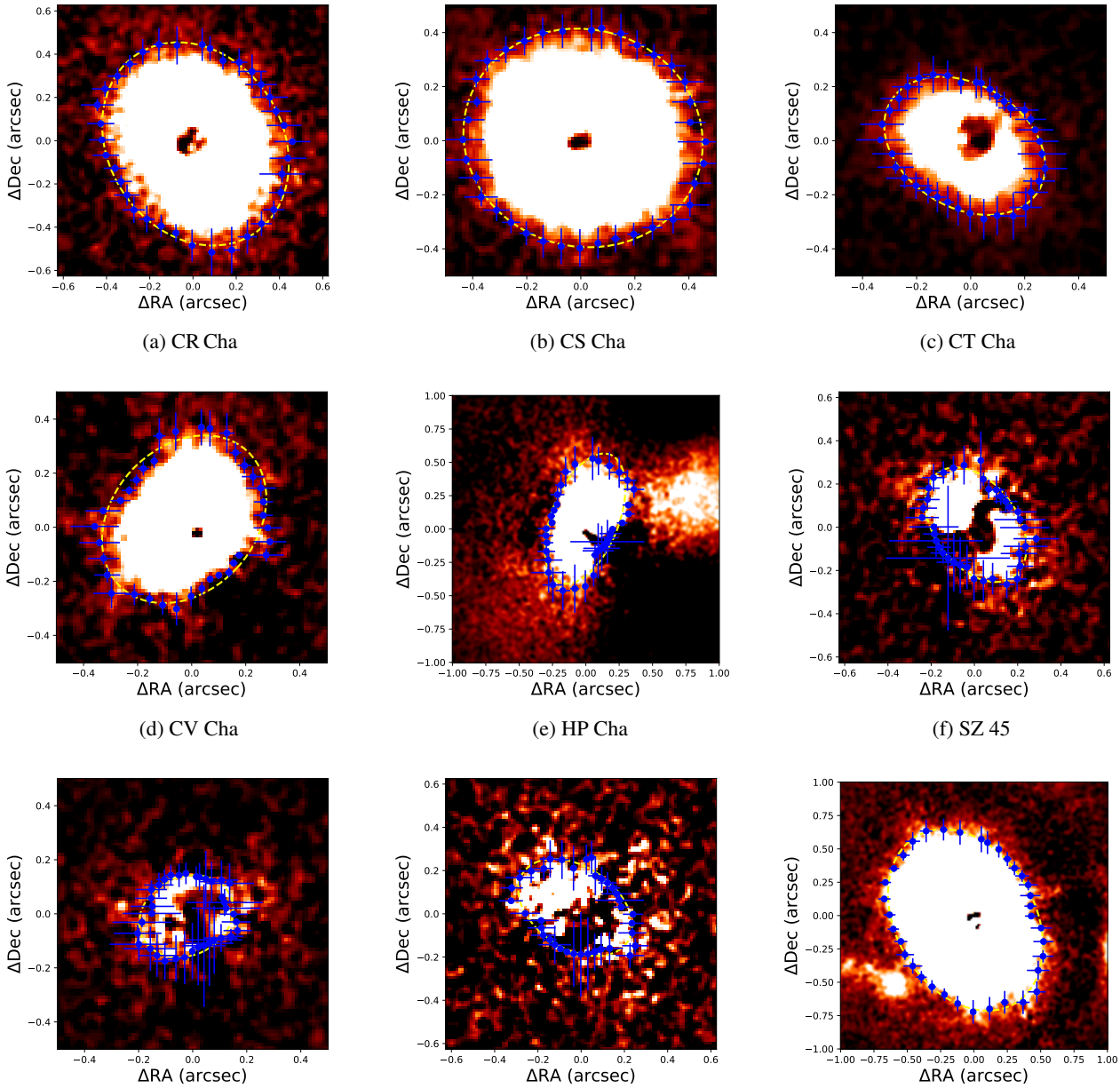

(a) CR Cha (b) CS Cha (c) CT Cha

(d) CV Cha (e) HP Cha (f) SZ 45

(g) TW Cha (h) VZ Cha (i) WW Cha

Fig. C.3: Ellipse fit to the outer disk edge in 5 of the 10 systems in this study. Disk images are shown on a saturated color map to highlight the edge, i.e. the region where disk signal drops below 3σ above the sky background. Yellow, dashed lines show the final fitted ellipse.

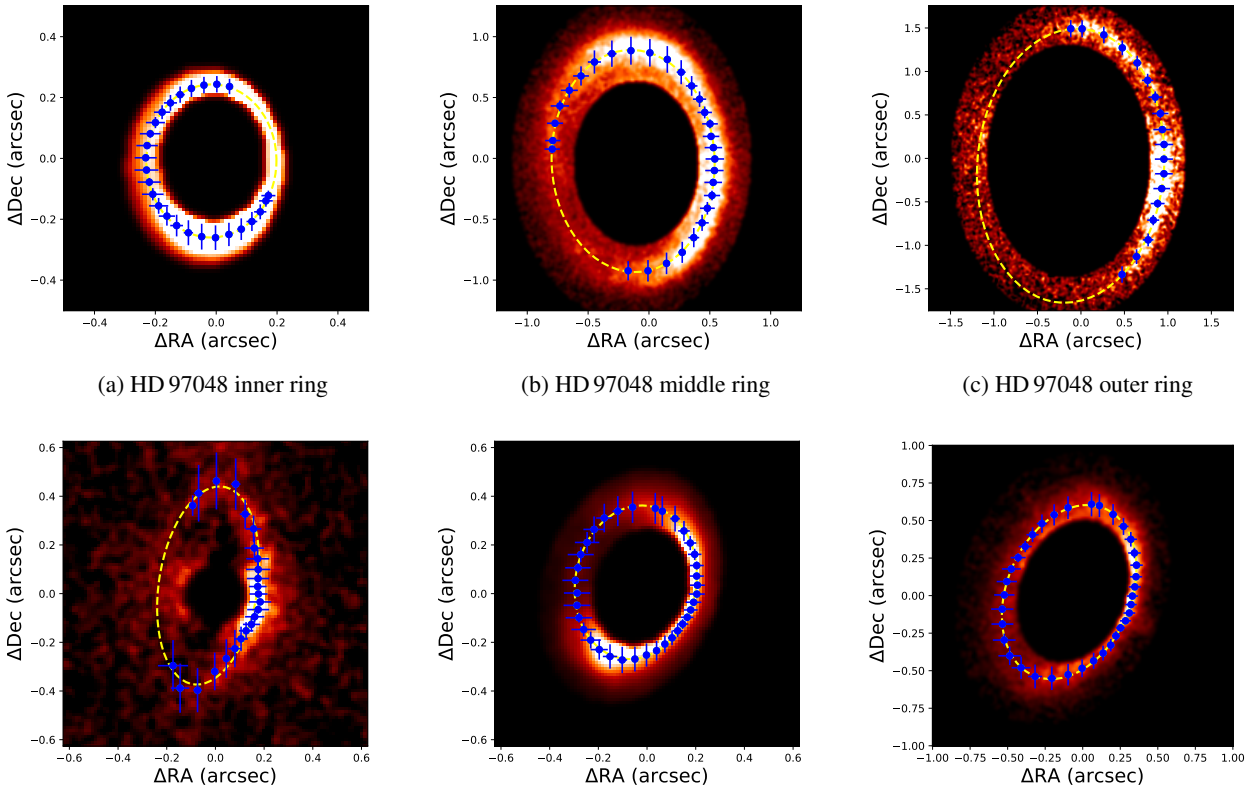

(a) HD 97048 inner ring (b) HD 97048 middle ring (c) HD 97048 outer ring

(d) SY Cha (e) SZ Cha inner ring (f) SZ Cha outer ring

Fig. C.4: Ellipse fit to the detected ring sub-structure in HD 97048, SY Cha and SZ Cha. Each ring was fitted individually while other features were masked. The displayed fitted ellipses (yellow dashed lines) represent the nominal best fit to the data, not taking into account any prior knowledge of the disk inclination and position angle.

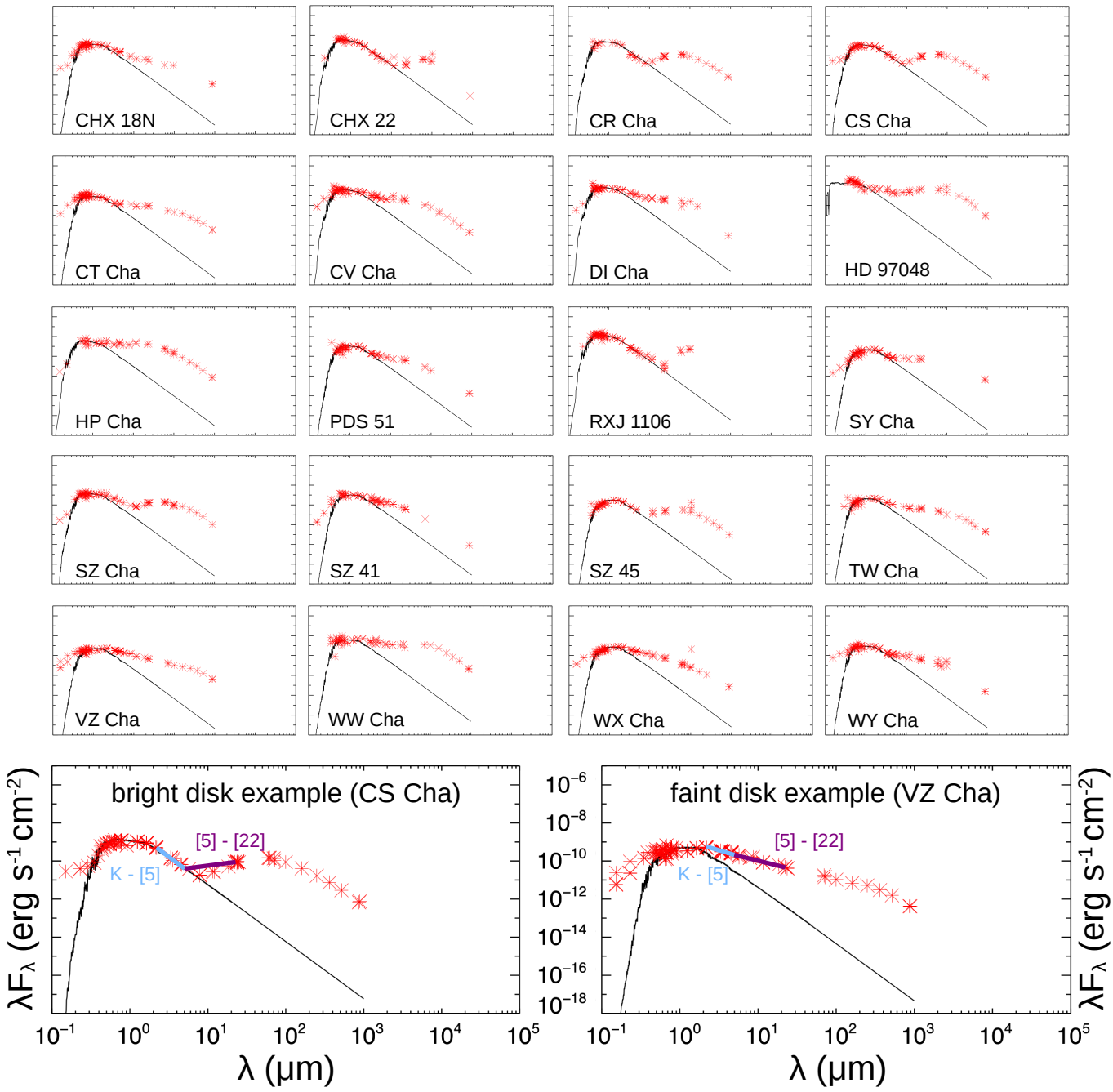

Fig. D.1: Spectral energy distributions for all our target systems. Photometric data points are marked in black (uncertainties are smaller than the symbol size). Red lines mark SPITZER/IRS spectra of the targets in the mid-IR, while green lines mark Herschel/SPIRE spectra in the far-IR.

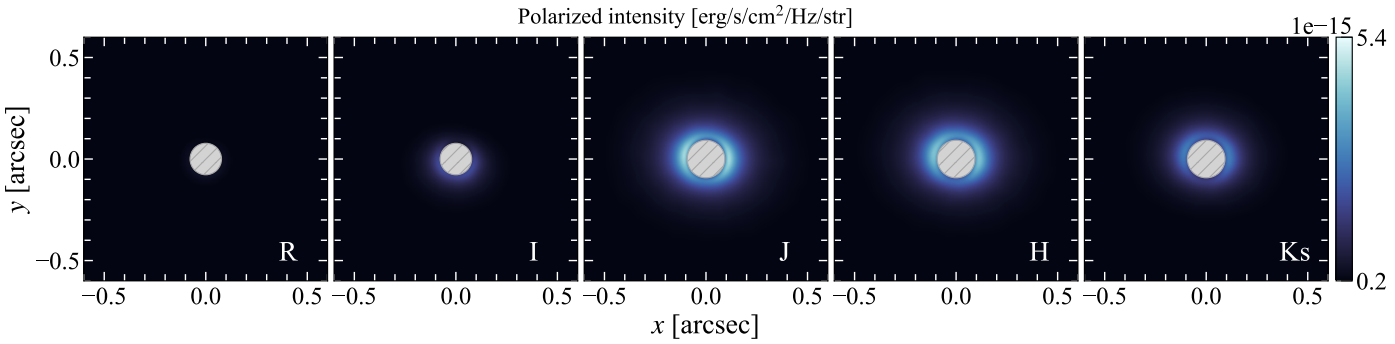

Fig. E.1: Radiative transfer models of CS Cha created with RADMC3d using compact dust grains with a maximum size of 0.32μm. The system inclination is set to 22° with a flaring exponent of the disk surface of 1.09. The models closely match the lack of forward scattering also absent in the data, as well as the sharp drop in brightness between the J-band and the I-band.

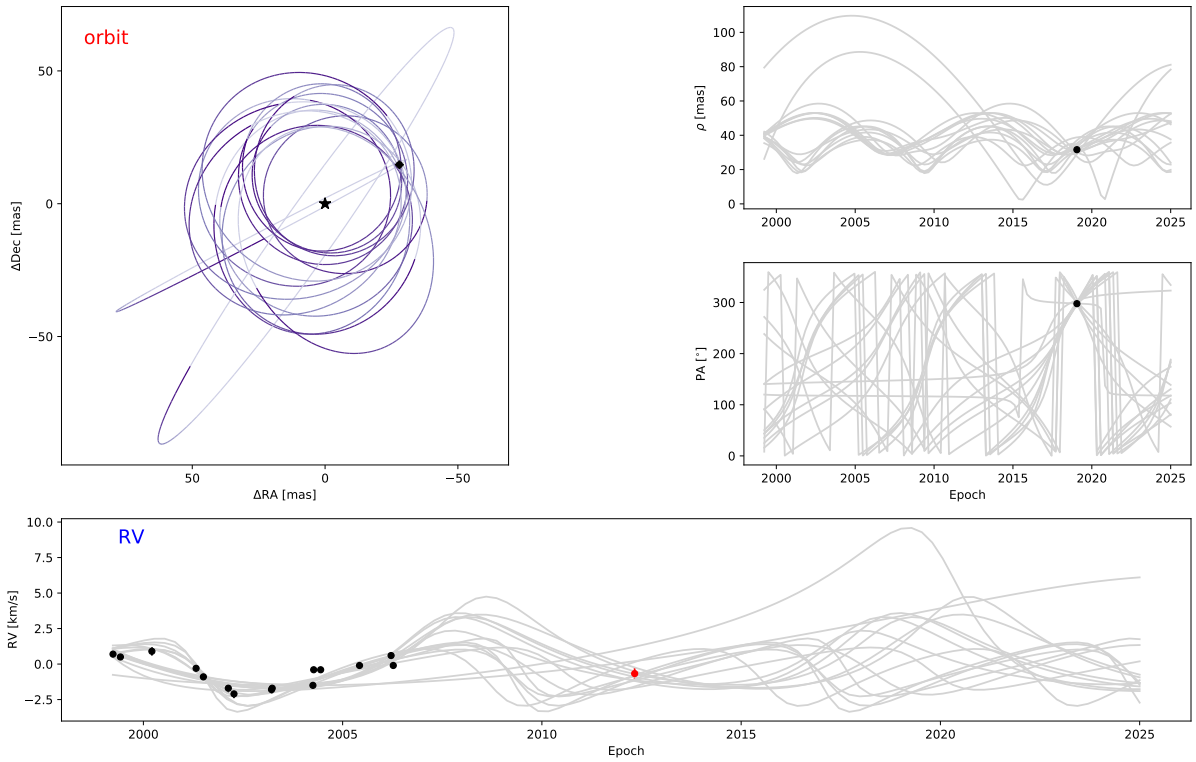

Fig. F.1: Results of *orbitize!* MCMC fit of the CS Cha stellar binary.

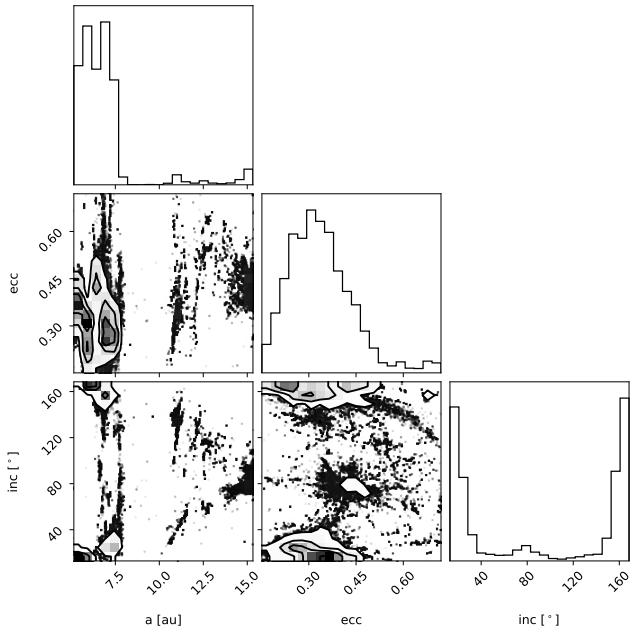

Fig. F.2: Results of *orbitize!* MCMC fit of the CS Cha stellar binary. Shown are the inclinations, eccentricities and semi-major axes of the resulting orbit distributions.